Universiteit Antwerpen

This item is the archived peer-reviewed author-version of:

On the causes of trends in the seasonal amplitude of atmospheric CO_2

Reference:

Piao Shilong, Liu Zhuo, Wang Yilong, Ciais Philippe, Yao Yitong, Peng Shushi, Chevallier Frederic, Friedlingstein Pierre, Janssens Ivan, Penuelas Josep, ...- On the causes of trends in the seasonal amplitude of atmospheric CO_2

Global change biology - ISSN 1354-1013 - 24:2(2018), p. 608-616

Full text (Publisher's DOI): https://doi.org/10.1111/GCB.13909

To cite this reference: https://hdl.handle.net/10067/1493030151162165141

uantwerpen.be

Institutional repository IRUA

On the causes of trends in the seasonal amplitude of atmospheric CO_2

Shilong Piao[1,2,3*], Zhuo Liu[1], Yilong Wang[4], Philippe Ciais[4], Yitong Yao[1], Shushi Peng[1], Frédéric Chevallier[4], Pierre Friedlingstein[5], Ivan A Janssens[6], Josep Peñuelas[7,8], Stephen Sitch[5], Tao Wang[2,3]

[1] Sino-French Institute for Earth System Science, College of Urban and Environmental Sciences, Peking University, Beijing 100871, China

[2] Key Laboratory of Alpine Ecology and Biodiversity, Institute of Tibetan Plateau Research, Chinese Academy of Sciences, Beijing 100085, China

[3] Center for Excellence in Tibetan Earth Science, Chinese Academy of Sciences, Beijing 100085, China

[4] Laboratoire des Sciences du Climat et de l'Environnement, CEA CNRS UVSQ, Gif-sur-Yvette, France

[5] College of Engineering, Computing and Mathematics, University of Exeter, Exeter EX4 4QF, UK

[6] Department of Biology, University of Antwerp, Universiteitsplein 1, 2610 Wilrijk, Belgium

[7] CREAF, Cerdanyola del Valles, Barcelona 08193, Catalonia, Spain.

[8] CSIC, Global Ecology Unit CREAF- CSIC-UAB, Bellaterra, Barcelona 08193, Catalonia, Spain.

Running title: Trends in atmospheric CO_2 amplitude

Keywords: Attribution, detection, amplitude of atmospheric CO_2, CO_2 fertilization effect, climate change, land use change

Manuscript for *Global Change Biology*

*** Corresponding author**

Paper type: Opinion

No consensus has yet been reached on the major factors driving the observed increase in the seasonal amplitude of atmospheric CO_2 in the northern latitudes. In this study, we used atmospheric CO_2 records from 26 northern hemisphere stations with a temporal coverage longer than 15 years, and an atmospheric transport model prescribed with net biome productivity (NBP) from an ensemble of nine terrestrial ecosystem models, to attribute change in the seasonal amplitude of atmospheric CO_2. We found significant ($P<0.05$) increases in seasonal peak-to-trough CO_2 amplitude (AMP_{P-T}) at nine stations, and in trough-to-peak amplitude (AMP_{T-P}) at eight stations over the last three decades. Most of the stations that recorded increasing amplitudes are in Arctic and boreal regions (>50 °N), consistent with previous observations that the amplitude increased faster at Barrow (Arctic) than at Mauna Loa (subtropics). The multi-model ensemble mean (MMEM) shows that the response of ecosystem carbon cycling to rising CO_2 concentration (eCO_2) and climate change are dominant drivers of the increase in AMP_{P-T} and AMP_{T-P} in the high latitudes. At the Barrow station, the observed increase of AMP_{P-T} and AMP_{T-P} over the last 33 years is explained by eCO_2 (39% and 42%) almost equally than by climate change (32% and 35%). The increased carbon losses during the months with a net carbon release in response to eCO_2 are associated with higher ecosystem respiration due to the increase in carbon storage caused by eCO_2 during carbon uptake period. Air-sea CO_2 fluxes (10% for AMP_{P-T} and 11% for AMP_{T-P}) and the impacts of land-use change (marginally significant 3% for AMP_{P-T} and 4% for AMP_{T-P}) also contributed to the CO_2 measured at Barrow, highlighting the role of these factors in regulating seasonal changes in the global carbon cycle.

Introduction

As an integrated signal of large scale ecological changes, the change in seasonal variations of atmospheric CO_2 concentration is an emerging property of the carbon cycle (Bacastow *et al.*, 1985; Kohlmaier *et al.*, 1989; Keeling *et al.*, 1996; Randerson *et al.*, 1997; Piao *et al.*, 2008; Graven *et al.*, 2013; Gray *et al.*, 2014; Zeng *et al.*, 2014; Barlow *et al.*, 2015; Forkel *et al.*, 2016; Wenzel *et al.*, 2016). The seasonal CO_2 amplitude (AMP) in the lower troposphere has increased by ≈ 50% north of 45°N since the 1960s (Graven *et al.*, 2013), and this signal has been suggested to be contributed by an increased seasonality of net biome productivity (NBP) in boreal and northern temperate ecosystems. A full understanding of the major factors governing the increase in NBP or the quantitative contribution of other, smaller fluxes such as fossil-fuel CO_2 emissions and air-sea exchange to the increase in AMP is still lacking. On the one hand, Gray *et al.* (2014) and Zeng *et al.* (2014) suggested that agricultural improvements contributed to the increase in AMP at Mauna Loa by increasing the seasonal NBP uptake in cultivated lands, but the estimated contribution of this mechanism differed two-fold between the two studies (range 17-45% of the increasing AMP). On the other hand, Randerson *et al.* (1997) and Forkel *et al.* (2016) showed that during the last three decades, most of the increase in amplitude took place at stations north of 55^{o}N. In this view, agriculture improvement seems unlikely to be the only driving factor, because croplands are mainly in northern temperate latitudes (Foley *et al.*, 2015). Using the LPJmL carbon cycle model with an improved phenological module coupled with an atmospheric transport model, Forkel *et al.* (2016) found that it is mainly the physiological

response of northern plants to warming rather to increasing CO_2 that explains the trend of AMP over the last 20 years, but Graven *et al.* (2013) showed that AMP increased in the 1960s to the mid-1970s at a time when northern temperature slightly decreased. Moreover, Barnes et al. (2016) suggested that advective fluxes through isentropic transport from mid-latitude surface fluxes play a larger impact than changes in Arctic fluxes on the northern high-latitude seasonal cycle throughout most of the troposphere, using GEOS-Chem chemical transport model with CO_2 fluxes simulated from CLM4.5. It therefore highlights the need to search deeper in the attribution of the AMP trend.

In this paper, we investigate the AMP trend in the Northern Hemisphere over the last thirty years (1980-2012) using an ensemble of ecosystem models with different parameterizations of the effects of elevated CO_2, climate change and land use change (TRENDYv2) (Sitch *et al.*, 2015) with another transport model (LMDZ4) (Hourdin *et al.*, 2013). We also separate the contribution of fossil fuel CO_2 emissions, air-sea fluxes as well as the effects of climate change, rising CO_2 concentration (eCO_2), land use change and nitrogen deposition in some models on the trends in the seasonality of land ecosystem carbon cycle. The contribution of atmospheric transport trends to AMP trends is also analyzed. We use long-term (>15 years during 1980-2012) trends in seasonal atmospheric CO_2 concentrations from 26 northern (north of 23°N) atmospheric stations of the NOAA-ESRL surface flask air-sampling network (Table S1 and Figure S1).

Materials and methods

Datasets

Atmospheric CO_2 concentration data. Weekly data for atmospheric CO_2 concentration were obtained for 1980-2012 from the archive of Earth System Research Laboratory, National Oceanic and Atmospheric Administration (NOAA-ESRL) (Masarie *et al.*, 2014). Our analyses used data from 26 northern temperate and boreal stations with observations longer than 15 years (Table S1), because the focus of our study was the long-term trend, which would not be robust without long-term observations. The seasonal curves of atmospheric CO_2 for each station were extracted by fitting the observation data with a function consisting of a quadratic polynomial for the long-term trend, four-harmonics for the annual cycle, and a 80-days Full-Width Half-Maximum value (FWHM) averaging filter and a 390-days FWHM averaging filter to further remove short term variations and remaining annual cycles still present in the residuals after the function fit (Thoning *et al.*, 1989). The processing was incorporated in the standard software for processing CO_2 data (CCGCRV) developed by NOAA-ESRL (Thoning *et al.*, 1989). We then obtained the amplitude and monthly concentration differences from the seasonal curve for atmospheric CO_2.

Land-atmosphere CO_2 exchange. An ensemble of eight dynamic global vegetation models (DGVMs) from TRENDYv2 was used to simulate monthly net biome productivity (NBP) for 1979-2012. These models were coordinated to perform three simulations (S1, S2 and S3) following the TRENDYv2 protocol (Sitch *et al.*, 2015). Only atmospheric CO_2 was varied in simulation S1, and only atmospheric CO_2 and climate were varied in simulation S2. In simulation S3, atmospheric CO_2, climate and land use were varied. The effects of rising

atmospheric CO_2, climate change and land use change on NBP could then be obtained from S1, the difference between S2 and S1, and the difference between S3 and S2, respectively. Four of the eight TRENDY models (CLM4.5, ISAM, LPX and OCN) considered carbon-nitrogen interactions and nitrogen deposition in simulation S1, S2 and S3. All models used the same forcing data sets, in which global atmospheric CO_2 concentration was from the combination of ice core records and atmospheric observations (Keeling *et al.*, 2005), historical climatic fields were from the CRU-NCEP dataset (http://dods.extra.cea.fr/data/p529viov/cruncep/), and land use data were from the Hyde database (Hurtt *et al.*, 2011). The effect of nitrogen deposition was derived from an additional simulation (S4) by the CLM4 model (Oleson *et al.*, 2010; Mao *et al.*, 2013) in which all driving factors (atmospheric CO_2, climate and land use) were kept constant at the 1980 value, except transient nitrogen deposition for 1980-2012 (Lamarque *et al.*, 2005). Strictly speaking, the effect of climate change on NBP contains the fingerprint of rising CO_2 since CO_2-induced climate change cannot be teased out based on offline simulations of carbon fluxes. The pure effect of climate change can only be obtained through resorting to the fully coupled earth system models (e.g. Mao *et al.*, 2017), however which exist a lot of biases in terms of the simulated climate fields, CO_2 concentration and other biogeochemical processes. Detailed information of the nine DGVMs used in this study is listed in Table S2.

Ocean-atmosphere CO_2 exchange. A biogeochemical model, PlankTOM5, combined with a global ocean general circulation model NEMO (NEMO-PlankTOM5), were used to simulate the physical, chemical and biological processes that affect the surface ocean CO_2

concentration and thus the ocean-atmosphere CO_2 exchange (Buitenhuis *et al.*, 2010). The PlankTOM5 model was forced by inputs of ions and compounds from river, sediment and dust (Cotrim *da Cunha et al.*, 2007; Aumont *et al.*, 2003). The NEMO model was driven by data for daily wind and precipitation from an NCEP reanalysis (Kalnay *et al.*, 1996). Further details can be found in Buitenhuis *et al.* (2010).

Fossil fuel CO_2 emissions. A gridded monthly time series of fossil fuel CO_2 emissions from CDIAC were constructed based on a proportional-proxy approach (Andres *et al.*, 2011; Boden *et al.*, 2016). Firstly, available monthly data for fossil fuel consumption data for 21 countries were compiled, which accounted for about 80% of global total emissions. These data were then used as a proxy for all remaining countries without monthly data based on countries' similarities in climates and economies (for few countries, geographic closeness was also considered). For some years without explicit monthly data, Monte Carlo methods were used to apply data from years with known monthly fractions to the years with missing-data. Further details can be found in Andres *et al.* (2011).

The atmospheric transport model. We used LMDZ4, a global tracer transport model (Hourdin *et al.*, 2013) driven by the re-analysis 3-D atmospheric wind fields from the European Centre for Medium-Range Weather Forecasts (Dee *et al.*, 2011), to transform land-atmosphere CO_2 exchange, fossil fuel CO_2 emission and ocean-atmosphere CO_2 exchange into point estimates of CO_2 concentration for the 26 stations. The model configuration we used had a horizontal spatial resolution of 3.75° longitude × 2.5° latitude with 19 vertical layers.

The effects of changes in atmospheric CO_2 ('CO_2'), climate ('CLIM'), land use ('LU'), fossil fuel ('FF'), ocean carbon flux ('Ocean') and atmospheric transport ('Wind') on seasonal change in atmospheric CO_2 concentration were differentiated by designing eight transport simulations (T1~T8, see Table S4). The first (T1) used time-varying monthly land-atmosphere CO_2 exchange under scenario S3 (driven by rising CO_2, climate change and land use change), fossil fuel CO_2 emission, and ocean-atmosphere CO_2 exchange coupled with the LMDZ4 transport model with variable winds, indicating the combined effects of 'CO_2', 'CLIM', 'LU', 'FF', 'Ocean' and 'Wind'. The LMDZ4 transport experiment was forced by historically varying wind but constant land-atmosphere CO_2 exchange, fossil fuel CO_2 emission and ocean-atmosphere CO_2 exchange for 1979 (T6) to assess the contribution of 'Wind'. The individual effects of 'CO_2', 'CLIM' and 'LU' were determined using the LMDZ4 model with varying winds to perform three more transport simulations (T2, T3 and T4, see Table 3), in which fossil fuel CO_2 emission and ocean-atmosphere CO_2 exchange were constant at the 1979 value but land-atmosphere CO_2 exchange varied under the three scenarios (S1, driven by CO_2; S2, driven by CO_2 and CLIM; S3, driven by CO_2, CLIM and LU). Consequently, the effect of 'CO_2' alone on seasonal CO_2 variation could be assessed by the difference between T2 and T6, that of 'CLIM' by the difference between T3 and T2, and that of 'LU' by the difference between T4 and T3. We also prescribed varying land-atmosphere CO_2 exchange from the CLM4 model under scenario S4 (varying only nitrogen deposition), constant fossil fuel CO_2 emission and ocean-atmosphere CO_2 exchange to the LMDZ4 model with constant winds (transport simulation T5) to obtain the effect of nitrogen deposition. Finally, we performed two more simulations in which only fossil fuel CO_2 emission or ocean-atmosphere

CO_2 exchange varied in addition to variable winds (T7 and T8) to obtain the individual effects of 'FF' and 'Ocean' on CO_2 seasonal variation. The contribution of 'FF' could thus be calculated from the difference between T7 and T6, and that of 'Ocean' from the difference between T8 and T6.

Observed CO_2 amplitude trends

The 26 northern (north of 23 ℃) atmospheric stations selected are shown in Figure S1 and Table S1. According to the shape of detrended CO_2 seasonal cycle (*Thoning et al.*, 1989) (see methods) (Figure S2), we divided the amplitude into peak-to-trough (AMP_{P-T}, defined as the difference between the peak and trough values of the CO_2 seasonal cycle in a year) and trough-to-peak (AMP_{T-P}, defined as the difference between the trough value of the CO_2 seasonal cycle in a year and the peak value of the cycle in the next year). The AMP_{P-T} and AMP_{T-P} represent the seasonal variations in atmospheric CO_2 concentration during the period of net carbon uptake and the period of net carbon release, respectively (Figure S2). Positive trends in AMP_{P-T} ranging from 0.05 to 0.15 ppm yr^{-1} are significant ($P<0.05$) at nine stations during 1980-2012, eight of which are north of 50 ℃ (Figure 1a). The other stations do not show significant positive AMP_{P-T} trends and five stations show negative trends (the latter being significant at only one station UUM). The significant increase in AMP_{P-T} mainly reflects an increasing CO_2 drawdown (defined by the monthly net change in CO_2 concentration) in June and July (Figure S3).

The trends in AMP_{T-P} reported in Table S1 are similar to those of $AMP_{P-T,}$ logically

expected because we remove a long-term mean trend in each CO_2 time series (Figure 1b). In total, seven out of the eight stations with a significant ($P<0.05$) increase in AMP_{T-P} during 1980-2012 are located north of 50 °N. The months of September and October are those during which most of the negative trend of AMP_{T-P} occurs at those stations (Figure S3). Overall, no stations show significant positive trend in AMP_{T-P} during the study period.

Terrestrial ecosystem model output and simulation of trends in CO_2 amplitude

The net biome productivity (NBP) from eight dynamic global vegetation models (DGVMs) from TRENDYv2 (Sitch *et al.*, 2015) and an additional model with carbon-nitrogen interactions (Oleson *et al.*, 2010; Mao *et al.*, 2013) (Table S2 and S3) are prescribed to the atmospheric transport model (LMDZ4) (Hourdin *et al.*, 2013) (See Methods). Time-varying monthly NBP of each model from TRENDYv2 under simulation S3 (driven by CO_2, climate change and land-cover change) (Sitch *et al.*, 2015), fossil fuel and cement emissions (Andres *et al.*, 2011; Boden *et al.*, 2016), and interannual air-sea fluxes (Buitenhuis *et al.*, 2010) were prescribed to the global LMDZ4 transport model (Hourdin *et al.*, 2013) with variable winds for 1980-2012. This simulation is the T1 (see Methods and Table S4), from which the modeled CO_2 concentration field was sampled at each station and analyzed changes in amplitude, as for the observed time series.

Most T1 simulations (except with the ISAM and JULES ecosystem models) produce a significant increase in AMP_{P-T} at boreal (north of 50 °N) stations (Figure 1a), though there are differences among models. In comparison with the observed average trend (0.094 ±

0.033 ppm yr^{-1}) of AMP_{P-T} at the eight boreal stations with a significant increase in AMP_{P-T}, three models show a larger AMP_{P-T} positive trend (CLM4.5: 0.105 ± 0.046 ppm yr^{-1}; LPJ: 0.101 ± 0.053 ppm yr^{-1}; VISIT: 0.101 ± 0.059 ppm yr^{-1}). The T1 simulations also correctly reproduced the absence of a trend for the three boreal stations with no significant trend in observed AMP_{P-T} (BAL, MHD and SHM in Figure 1a), except for ORCHIDEE for MHD and VISIT for SHM.

Similar to trends in AMP_{P-T}, statistically significant increasing AMP_{T-P} is found in the T1 simulation results (except again for ISAM and JULES), consistent with the observed trends. The simulations with ISAM and JULES produce more significant increasing trends in AMP_{T-P} for temperate than boreal and Arctic stations.

Overall, unlike previous studies that have shown a systematic underestimation of AMP trend by ecosystem models, namely the CMIP5 models (Taylor *et al.*, 2012) and the MsTMIP models (Huntzinger *et al.*, 2013; Wei *et al.*, 2014) at high northern latitudes (Graven *et al.*, 2013; Thomas *et al.*, 2016), we found both underestimation and overestimation of AMP trends from the TRENDYv2 models (Figure S4). This phenomenon may be due to different climate forcing (between CMIP5 and other ensembles), partly different terrestrial ecosystem models, and the simulation of transport using different models (LMDZ4 here instead of TM3 and ACTM in Graven *et al.* (2013) and TM3 in Thomas *et al.* (2016)).

Effects of various factors on the trends in AMP_{P-T}

In order to separate the contribution of different driving factors on the trend of AMP_{P-T}, we performed transport simulations with changes in NBP caused by different factors from factorial runs of the TRENDYv2 models, respectively with variable CO_2 only (eCO_2), variable CO_2 and climate, and variable CO_2, climate and land cover change (Table S4, see Methods). We further differentiated between the contribution of trends in atmospheric transport from the trends in AMP, using the LMDZ4 transport model with variable transport fields (Dee *et al.*, 2011) but constant NBP, air-sea CO_2 flux and fossil fuel and cement emissions for 1979, so that the trends in AMP from this simulation could be attributed to transport trends only.

The impact of climate change on NBP affecting the AMP_{P-T} trends estimated from the multi-model ensemble mean (MMEM) varies among stations (Figure 2a). We find a positive trend of AMP induced by climate change at boreal atmospheric stations (eight of 11 stations north of 50 ºN (Figure 2a and S5b). On average, climate change caused an enhancement of 0.015 ± 0.025 ppm yr^{-1} in AMP_{P-T} over boreal region (north of 50 ^{o}N) (Figure 3a), which is about 20% of the observed AMP_{P-T} trend. To have an idea of the potential impact of different climatic factors, we present an analysis on the trends of temperature and precipitation during 1980-2012 in northern hemisphere. As shown in Figure S5, most northern high-latitude regions show non-significant trends of precipitation. By contrast, a positive trend of temperature was widely found in eastern Siberia and Alaska (Figure S5), which is also the main footprint area of Barrow station (Piao *et al.*, 2017). This result indicates that

temperature is the possible dominant factor on AMP trends at high latitudes, although such positive effects may saturate (Piao *et al.*, 2014; Fu *et al.*, 2015). As shown in Figure S6a, for the BRW station (71 ^{o}N), the effect of climate change on AMP_{P-T} is positive mainly during May and June.

In contrast, at the temperate stations (in the band of 23-50 ^{o}N), the effect of climate change on the AMP_{P-T} trends is mainly negative (10 of the 15 stations), although the impact is not significant (except for TAP at $P<0.05$ and ASK marginally significant at $P<0.1$). Climate change is modeled to cause an average decrease in AMP_{P-T} of -0.012 ± 0.040 ppm yr^{-1} at stations in the temperate region (Figure 3a). Analysis of NBP impacted by climate change (Trendy models S2 – S1 simulations) shows that climate change alone caused a decrease in CO_2 uptake from April to August in western and central US, eastern Europe, northeast China and Mongolia (Figure S7b), associated with declining soil moisture driven by rising temperature and decreasing precipitation in these regions (Sitch *et al.*, 2015).

In the simulations of CO_2 with MMEM, eCO2 causes a significant increase in AMP_{P-T} at 10 of the 11 boreal stations (Figure 2a), and the magnitude of trend in AMP_{P-T} driven by eCO2 (0.036 ± 0.005 ppm yr^{-1}) is about twice as large as that caused by climate change (Figure 3a). This larger effect of eCO2 than climate change on the AMP_{P-T} trends in the boreal zone is also present in the simulations with NBP in the individual ecosystem models (Figure S8a and b). This result does not support previous findings by Forkel *et al.* (2016), in which the signal of climate change is considered larger than eCO2 in the observed increase

of AMP_{P-T} at high latitudes. We agree, however, that climate change rather than eCO2 causes the latitudinal difference of trend in AMP_{P-T}. The magnitude of eCO2 effect to increase the trend of AMP in temperate regions (0.028 ± 0.023 ppm yr^{-1}) is comparable to that in boreal regions (Figure 3a), although the effect is sigficant at fewer stations (nine of 15) (Figure 2a). It should be noted that four TRENDY models (CLM4.5, ISAM, LPX and OCN) considered carbon-nitrogen interactions and nitrogen deposition, thus the eCO_2 signal derived from these models also includes the interactive effect of nitrogen deposition. Another simulation with nitrogen deposition using the CLM4 model (Oleson *et al.*, 2010; Mao *et al.*, 2013) (see Methods), howeever, predicts that the effect of nitrogen deposition on the AMP_{P-T} trend is not significant ($P<0.05$) at any of the stations (Figure S9a), but this result depends on individual model parameterizations (Galloway *et al.*, 2008). Further studies based on multiple models with carbon-nitrogen interactions are thus needed.

Both forest inventory data and model simulation have indicated that afforestation and forest regrowth after the abandonment of agriculture in northern ecosystems have an important role in regional and global carbon balances (Pan *et al.*, 2011; Houghton *et al.*, 2012; FAO, 2015). Most TRENDYv2 DGVMs (except ISAM) in our study predict that land use change would increase net carbon uptake from April to August in Eastern Europe, China and central and eastern United States (Figure S7c). Accordingly, a significant ($P<0.05$) or marginally significant ($P<0.10$) positive effect of land use change on the trend in AMP_{P-T} is predicted across six boreal stations and three northern temperate stations (Figures 2a and S5c), although the magnitude of the signal is generally much smaller than the effect of eCO_2

and climate change. Overall, the positive increase in AMP_{P-T} attributed to land use change is similar between boreal (0.007 ± 0.009 ppm yr^{-1}) and northern temperate (0.004 ± 0.008 ppm yr^{-1}) regions (Figure 3a), suggesting that the latitudinal difference in observed AMP_{P-T} increase (0.07 ± 0.05 ppm yr^{-1} in the boreal zone and 0.01 ± 0.05 ppm yr^{-1} in temperate zone) has little linkage with land use change. It should be noted that, however, large uncertainties remain in estimating the effect of land use change on the AMP_{P-T} trend, primarily because processes of land use change and management (e.g., wood harvest, shifting cultivation and peat fires) are not considered in some Trendy models (Table S3) and some critical processes (e.g., human settlement, erosion/sequestration and woody encroachment) are absent in all models (Houghton *et al.*, 2012).

Over the past thirty years, global CO_2 emissions from fossil fuel consumption have increased from 5.3 Pg C yr^{-1} in 1980 to 9.7 Pg C yr^{-1} in 2012 (Boden *et al.*, 2016) (Figure S10a). However, the pattern of change is not spatially uniform in the Northern Hemisphere. Annual fossil fuel CO_2 emissions is increased significantly in the northern temperate region, but decreased in the boreal region (Figure S10a). This heterogeneity is also found in the period of April to August, during which AMP_{P-T} is calculated for most northern temperate and boreal stations (Figure S10b). As a result, effect of changes in fossil fuel carbon emissions on the trend in AMP_{P-T} is opposite between temperate and boreal stations, although the trends in AMP_{P-T} caused by the trends in fossil CO_2 emissions were not significant for most stations. A negative effect of fossil fuel emissions on the AMP_{P-T} trend is simulated for the temperate stations (13 of the 15 stations showing a negative trend with

three significant stations and one marginally significant station) (Figue 2a), and a positive effect is simulated for most boreal stations (eight of the 11 stations). The absolute value of the $AMP_{P\text{-}T}$ trend associated with fossil fuel emissions is generally larger at temperate (average of -0.013±0.022 ppm yr^{-1}) compared to boreal stations (average of 0.003±0.007 ppm yr^{-1}) (Figure 3a).

A recent study (Horton *et al.*, 2015) demonstrated robust trends in sub-seasonal atmospheric circulation patterns over mid-latitude regions during 1979-2013, particularly in summer and autumn. Such changes in large-scale atmospheric circulation may exert an effect on the trend of CO_2 amplitude. The magnitude of $AMP_{P\text{-}T}$ trend caused by transport change is comparable or even larger than the effect of climate change and eCO_2 on NBP at some atmospheric stations, particularly in the temperate zone, although the impact of transport trends on the trend in $AMP_{P\text{-}T}$ was significant for only two stations (UUM and IZO) (Figure 2a). The magnitude of $AMP_{P\text{-}T}$ trend caused by wind is remarkable at UUM (Figure 2a), suggesting the potential role of atmospheric transport. This result is consistent with the recent study showing that increasing seasonal fluxes in lower latitudes have a larger impact on the CO_2 amplitude throughout most of the troposphere compared to increasing seasonal fluxes at higher latitudes due to isentropic transport across latitudes (Barnes *et al.*, 2016).

In terms of effects air-sea fluxes on the trend of $AMP_{P\text{-}T}$, a weak contribution to AMP trends was simulated across most of stations except at BRW (0.010 ppm yr^{-1}, $P<0.05$, 10% of the observed trend) and MBC (0.015 ppm yr^{-1}, $P<0.1$, 16% of the observed trend).

The mechanisms driving the trend in AMP_{P-T} are here analyzed with observations at the Arctic station of BRW (71°N), the longest northern high latitude CO_2 record showing an increase of amplitude of 35% since 50 years, larger than at the Mauna Loa longest record located in the sub-tropics (Graven *et al.*, 2013; Gray *et al.*, 2014; Zeng *et al.*, 2014; Barlow *et al.*, 2015; Forkel *et al.*, 2016). Our transport simulations with MMEM NBP indicate that AMP_{P-T} at the BRW station significantly increased by about 0.095 ppm yr^{-1} from 1980 to 2012, comparable to the observed trend of 0.097 ppm yr^{-1} (Figure 1a). eCO_2 is identified as the largest contributor of increasing AMP_{P-T} with a trend of 0.039 ppm yr^{-1} (40% of the observed trend, $P<0.05$), followed by climate change with a trend of 0.031 ppm yr^{-1} (32% of the observed trend, $P<0.05$) (Figure S8a and b). The effect of ocean flux is of 0.010 ppm yr^{-1} (10% of observed trend, $P<0.05$), and land use change has marginally significant contributions (0.003 ppm yr^{-1} and 3% of observed trend, $P<0.1$) (Figure S8c and e). The impacts on the AMP_{P-T} trend were not significant for the other factors such as fossil fuel emissions and transport (Figure S8d and f).

Effects of various factors on trends in AMP_{T-P}

We also assessed the effect of various factors on the trend in AMP_{T-P} with the same NBP and transport model simulations (See Methods). In contrast to the period of net carbon uptake, climate change accelerates carbon release from boreal ecosystems during the non-carbon uptake period. An increasing AMP_{T-P} (a negative trend in AMP_{T-P} indicates a larger release) is simulated at eight of the 11 boreal stations (one station significant at $P<0.05$;

two stations marginally significant at P<0.1; Figure 2b). In contrast, a decreasing AMP_{T-P} (shown with positive trend) is produced at 12 of the 15 temperate stations (one station significant at P <0.05; one station marginally significant at P<0.1) (Figure 2b). Autumnal warming may increase vegetation productivity by delaying vegetation senescence, as well as accelerate ecosystem respiration (Piao *et al.*, 2008; Vesala *et al.*, 2010). The opposite effect of climate change on the trend in AMP_{T-P} in boreal (-0.016 ± 0.027 ppm yr^{-1}) and temperate (0.011 ± 0.040 ppm yr^{-1}) regions (Figure 3b) is therefore probably due to their different magnitudes of the response of vegetation productivity (GPP) and ecosystem respiration (TER) to climate change. Indeed, the model show that the climate change induced increase of TER is greater than that of GPP in high northern latitudes, whereas the increase of GPP is larger in temperate regions (Figure S11).

Simulation of atmospheric CO_2 from MMEM NBP produce an increasing AMP_{T-P} in response to eCO_2 at 25 of the 26 temperate and boreal stations (19 stations significant at P<0.05, two stations marginally significant at 0.05<P<0.1; Figure 2b). NBP from six out of the eight terrestrial ecosystem models (except ISAM and JULES) also produces an enhancing AMP_{T-P} from eCO2 (Figure S12a). This result indicates that an acceleration of carbon release during the period of net carbon release is as an indirect effect of the NBP response to eCO2. This acceleration is due to the increment in carbon storage caused by the enhancement of net carbon uptake during the period of carbon uptake under the effect of eCO_2, which stimulates ecosystem respiration during the non-carbon uptake period (Figure S13). Similarly, we also found enlargement of AMP_{T-P} in response to land use change

(significant at nine of the 26 stations, Figure 2b).

Similar to the effect on AMP_{P-T}, the contribution of fossil fuel CO_2 emissions, air-sea fluxes and transport on the trends in AMP_{T-P} are significant only at a minority of stations (only one, four and two stations at $P<0.05$ for the effect of fossil fuel, air-sea fluxes and transport, respectively; Figure 2b). However, the magnitude of signal induced by transport and fossil fuel emissions is generally remarkable over temperate region (Figure 3b), causing an average impacts of -0.014 ± 0.036 ppm yr^{-1} and 0.010 ± 0.014 ppm yr^{-1} in the trend of AMP_{P-T}, respectively.

Overall, the observed significant enlargement of AMP_{T-P} at the BRW station (-0.090 ppm yr^{-1}) is mainly driven by eCO2 (-0.038 ppm yr^{-1} and 42% of the observing trend, $P<0.05$), climate change (0.032 ppm yr^{-1} and 35% of the observing trend, $P<0.05$), ocean flux change (-0.010 ppm yr^{-1} and 11% of the observing trend, $P<0.05$) and land use change (-0.003 ppm yr^{-1} and 4% of the observing trend, $P<0.05$).

Conclusion

Unlike previous studies based on one model only (Zeng *et al.*, 2014; Forkel *et al.*, 2016), our results based on an ensemble of models to capture the trends in amplitude suggest that rising atmospheric CO_2 concentration is the primary driver of enhancement of both AMP_{P-T} and AMP_{T-P}**,** although climate change plays a critical role and contributes largely to the latitudinal differences in the AMP trend. In addition, the effects of other factors such as land

use change, fossil fuel emissions, ocean flux, and transport on the trends in AMP_{P-T} and AMP_{T-P} are not statistically significant at most stations, but still large enough to cancel out the effect of eCO_2 at some temperate stations where the observed seasonal CO_2 trends are small. However, the uncertainties in the forcing data on land use change and fossil fuel emission at the moment do not allow an unequivocal statement on the contribution of these factors, and further studies based on spatially and temporally explicit historical data sets, including land use and fossil fuel emission are needed. Finally, rising atmospheric CO_2 concentration has an opposite implication in the northern ecosystem carbon balance between the period of carbon uptake (trend in AMP_{P-T}) and the period of carbon release (trend in AMP_{P-T}), due to the lagged effects of increases in carbon storage during the period of carbon uptake on the carbon cycle in the period of carbon release. Our results not only provide insights for large-scale field experiments, but also highlight the importance of understanding processes of the carbon release during the non-growing season, which is critical for reliable projections of the global carbon cycle, and thus, the future climate change.

Acknowledgments

We thank the TRENDY modelers for contributing the model outputs. This study was supported by the National Natural Science Foundation of China (41530528), the BELSPO STEREO project ECOPROPHET (SR00334), the 111 Project (B14001), and the National Youth Top-notch Talent Support Program in China. Philippe Ciais, Ivan A Janssens and Josep Peñuelas acknowledge support from the European Research Council through Synergy grant ERC-2013-SyG-610028 “P-IMBALANCE”.

References

Andres RJ, Gregg JS, Losey L, Marland G, Boden TA (2011) Monthly, global emissions of carbon dioxide from fossil fuel consumption. *Tellus,* **63B**, 309-327.

Aumont O, Maier-Reimer E, Blain S, Monfray P (2003) An ecosystem model of the global ocean including Fe, Si, P colimitations. *Global Biogeochemical Cycles,* **17**, 1060, doi:10.1029/2001GB001745.

Bacastow RB, Keeling CD, Whorf TP (1985) Seasonal amplitude increase in atmospheric CO_2 concentration at Mauna Loa, Hawaii, 1959–1982. *Journal of Geophysical Research: Atmospheres,* **90**, 10529-10540.

Barlow JM, Palmer PI, Bruhwiler LM, Tans P (2015) Analysis of CO_2 mole fraction data: first evidence of large-scale changes in CO_2 uptake at high northern latitudes. *Atmospheric Chemistry and Physics,* **15**, 13739-13758.

Barnes EA, Parazoo N, Orbe C, Denning AS (2016). Isentropic transport and the seasonal cycle amplitude of CO_2, *J. Geo- phys. Res. Atmos.* **121**, 8106–8124, doi:10.1002/2016JD025109.

Boden TA, Marland G, Andres RJ (2016) Global, regional, and national fossil-fuel CO_2 Emissions. Carbon Dioxide Information Analysis Center, Oak Ridge National Laboratory, U.S. Department of Energy, Oak Ridge, Tenn., U.S.A. doi 10.3334/CDIAC/00001_V2016.

Buitenhuis ET, Rivkin RB, Sailley S, Le Quéré C (2010) Biogeochemical fluxes through microzooplankton. *Global Biogeochemical Cycles,* **24**, GB4015,

doi:10.1029/2009GB003601.

Clark DB, Mercado LM, Sitch S *et al*. (2011) The Joint UK Land Environment Simulator (JULES), model description-Part 2: carbon fluxes and vegetation dynamics. *Geoscientific Model Development*, **4**, 701-722.

Cotrim da Cunha L, Buitenhuis ET, Le Quéré C, Giraud X, Ludwig W (2007) Potential impact of changes in river nutrient supply on global ocean biogeochemistry. *Global Biogeochemical Cycles*, **21**, GB4007, doi:10.1029/2006GB002718.

Dee DP, Uppala SM, Simmons AJ *et al*. (2011) The ERA-Interim reanalysis: configuration and performance of the data assimilation system. *Quarterly Journal of the royal meteorological society*, **137**, 553-597.

Foley JA, DeFries R, Asner GP *et al*. (2005) Global consequences of land use. *Science*, **309**, 570-574.

Food and Agriculture Organization of the United States (FAO) (2015). Global Forest Resources Assessment 2015: How are the world's forests changing? http://www.fao.org/forest-resources-assessment/en/.

Forkel M, Carvalhais N, Rödenbeck C *et al*. (2016) Enhanced seasonal CO_2 exchange caused by amplified plant productivity in northern ecosystems. *Science*, **351**, 696-699.

Fu YH, Zhao H, Piao S *et al*. (2015) Declining global warming effects on the phenology of spring leaf unfolding. *Nature*, **526**, 104–107.

Galloway JN, Townsend AR, Erisman JW *et al*. (2008) Transformation of the nitrogen cycle: recent trends, questions, and potential solutions. *Science*, **320**, 889-892.

Graven HD, Keeling RF, Piper SC *et al*. (2013) Enhanced seasonal exchange of CO_2 by northern ecosystems since 1960. *Science,* **341**, 1085-1089.

Gray JM, Frolking S, Kort EA *et al*. (2014) Direct human influence on atmospheric CO_2 seasonality from increased cropland productivity. *Nature,* **515**, 398-401.

Horton DE, Johnson NC, Singh D *et al*. (2015) Contribution of changes in atmospheric circulation patterns to extreme temperature trends. *Nature,* **522**, 465-469.

Houghton RA, House JI, Pongratz J *et al*. (2012) Carbon emissions from land use and land-cover change. *Biogeosciences,* **9**, 5125-5142.

Hourdin F, Foujols MA, Codron F *et al*. (2013) Impact of the LMDZ atmospheric grid configuration on the climate and sensitivity of the IPSL-CM5A coupled model. *Climate Dynamics,* **40**, 2167-2192.

Huntzinger DN, Schwalm C, Michalak AM *et al*. (2013) The North American Carbon Program Multi-Scale Synthesis and Terrestrial Model Intercomparison Project - Part 1: Overview and experimental design. *Geoscientific Model Development,* **6**, 2121-2133.

Hurtt GC, Chini LP, Frolking S *et al*. (2011) Harmonization of land-use scenarios for the period 1500-2100: 600 years of global gridded annual land-use transitions, wood harvest, and resulting secondary lands. *Climatic change,* **109**, 117-161.

Jain AK, Meiyappan P, Song Y, House JI (2013) CO_2 emissions from land-use change affected more by nitrogen cycle, than by the choice of land-cover data. *Global change biology,* **19**, 2893-2906.

Kalnay E, Kanamitsu M, Kistler R *et al* (1996) The NCEP/NCAR 40-year reanalysis project. *Bulletin of the American meteorological Society,* **77**, 437-471.

Kato E, Kinoshita T, Ito A, Yamagata Y (2013) Evaluation of spatially explicit emission scenario of land-use change and biomass burning using a process-based biogeochemical model. *Journal of Land Use Science,* **8**, 104-122.

Keeling, CD, Chin JFS, Whorf TP (1996) Increased activity of northern vegetation inferred from atmospheric CO_2 measurements. *Nature,* **382**, 146–149.

Keeling CD, Whorf TP (2005) Atmospheric carbon dioxide record from Mauna Loa. Trends: A Compendium of Data on Global Change. Carbon Dioxide Information Analysis Center, Oak Ridge National Laboratory, Oak Ridge, TN.

Kohlmaier GH, Sir é E, Janecek A, Keeling CD, Piper SC, Revelle R (1989) Modelling the seasonal contribution of a CO_2 fertilization effect of the terrestrial vegetation to the amplitude increase in atmospheric CO_2 at Mauna Loa Observatory. *Tellus,* **41B**, 487-510.

Krinner G, Viovy N, de Noblet‐Ducoudr é N *et al*. (2005) A dynamic global vegetation model for studies of the coupled atmosphere-biosphere system. *Global Biogeochemical Cycles,* **19**, 1-33.

Lamarque JF, Kiehl JT, Brasseur GP *et al*. (2005) Assessing future nitrogen deposition and carbon cycle feedback using a multimodel approach: Analysis of nitrogen deposition. *Journal of Geophysical Research: Atmospheres,* **110**, D19303, doi:10.1029/2005JD005825.

Mao J, Shi X, Thornton PE *et al*. (2013) Global latitudinal-asymmetric vegetation growth trends and their driving mechanisms: 1982–2009. *Remote Sensing,* **5**, 1484-1497.

Mao J, Ribes A, Yan B *et al.* (2017) Human-induced greening of the northern extratropical

land surface. *Nature Climate Change* **6**, 959-963.

Masarie KA, Peters W, Jacobson AR, Tans PP (2014) ObsPack: a framework for the preparation, delivery, and attribution of atmospheric greenhouse gas measurements. *Earth System Science Data,* **6**, 375-384.

Oleson KW, Lawrence DM, Gordon B *et al*. (2010) Technical description of version 4.0 of the Community Land Model (CLM). NCAR Technical Note NCAR/TN 478+STR; The National Center for Atmospheric Research (NCAR): Boulder, Colorado.

Oleson KW, Lawrence DM, Gordon B *et al*. (2013) Technical Description of version 4.5 of the Community Land Model (CLM). NCAR Technical Note NCAR/TN 503+STR; The National Center for Atmospheric Research (NCAR): Boulder, Colorado.

Pan Y, Birdsey RA, Fang J *et al*. (2011) A large and persistent carbon sink in the world's forests. *Science,* **333**, 988-993.

Piao S, Ciais P, Friedlingstein P *et al*. (2008) Net carbon dioxide losses of northern ecosystems in response to autumn warming. *Nature,* **451**, 49-52.

Piao S, Nan H, Huntingford C *et al*. (2014) Evidence for a weaking relationship between interannual temperature variability and northern vegetataion activity. *Nature communications,* **5,** doi:10.1038/ncomms6018.

Randerson, JT, Thompson MV, Conway TJ, Fung IY, Field CB (1997) The contribution of terrestrial sources and sinks to trends in the seasonal cycle of atmospheric carbon dioxide. *Global Biogeochemical Cycles,* **11**, 535-560.

Sitch S, Smith B, Prentice IC *et al*. (2003) Evaluation of ecosystem dynamics, plant geography and terrestrial carbon cycling in the LPJ dynamic global vegetation model.

Global Change Biology, **9**, 161-185.

Sitch S, Friedlingstein P, Gruber N *et al*. (2015) Recent trends and drivers of regional sources and sinks of carbon dioxide. *Biogeosciences,* **12**, 653–679.

Stocker BD, Roth R, Joos F *et al*. (2013) Multiple greenhouse-gas feedbacks from the land biosphere under future climate change scenarios. *Nature Climate Change,* **3**, 666-672.

Taylor KE, Stouffer RJ, Meehl GA (2012) An Overview of CMIP5 and the Experiment Design. *Bulletin of the American Meteorological Society,* **93**, 485-498.

Thomas R, Prentice IC, Graven H *et al*. (2016) CO_2 and greening observations indicate increasing light use efficiency in northern terrestrial ecosystems. *EGU General Assembly Conference Abstracts*, **18**, 14335.

Thoning KW, Tans PP, Komhyr WD (1989) Atmospheric carbon dioxide at Mauna Loa observatory. II- Analysis of the NOAA GMCC data, 1974-1985. *Journal of Geophysical Research,* **94,** 8549-8565.

Vesala T, Launiainen S, Kolari P *et al*. (2010) Autumn temperature and carbon balance of a boreal Scots pine forest in Southern Finland. *Biogeosciences,* **7**, 163-176.

Wei Y, Liu S, Huntzinger DN *et al*. (2014) The North American Carbon Program Multi-Scale Synthesis and Terrestrial Model Intercomparison Project: Part 2 - Environmental Driver Data. *Geoscientific Model Development,* **7**, 2875-2893.

Wenzel S, Cox PM, Eyring V, Friedlingstein P (2016) Projected land photosynthesis constrained by changes in the seasonal cycle of atmospheric CO_2. *Nature*, **538**, 499-501.

Zaehle S, Friend AD (2010) Carbon and nitrogen cycle dynamics in the O-CN land surface model: 1. Model description, site-scale evaluation, and sensitivity to parameter estimates.

Global Biogeochemical Cycles, **24**, doi:10.1029/2009GB003521.

Zeng N, Zhao F, Collatz GJ *et al*. (2014) Agricultural Green Revolution as a driver of increasing atmospheric CO_2 seasonal amplitude. *Nature*, **515**, 394-397.

Supporting Information Captions

Tables

Table S1 Atmospheric CO_2 measurement stations (data coverage > 15 years in the period of 1980-2012) used in the study and estimated trends of peak-to-trough amplitude (AMP_{P-T}) and trough-to-peak amplitude (AMP_{T-P}).

Table S2 Details of dynamic global vegetation models used in this study.

Table S3 Processes of land use change and management considered in TRENDYv2 models.

Table S4 Summary of transport simulations performed.

Figures

Figure S1 Spatial distribution of the NOAA-ERSL stations (data coverage > 15 years) used in this study.

Figure S2 A schematic describing the terms we used to characterize the seasonal amplitude of atmospheric CO_2.

Figure S3 Observed trends in monthly net CO_2 concentration change (MNCC) from long-term records of the global NOAA-ERSL surface flask air-sampling network.

Figure S4 Observed and modeled trends in CO_2 seasonal peak-to-trough amplitude (AMP_{P-T}) (a, c) and trough-to-peak amplitude (AMP_{T-P}) (b, d) during 1980 to 2012, averaged over the stations from northern temperate region (23-50^{o}N) and boreal region (north of 50^{o}N).

Figure S5 Spatial distribution of trends in temperature (a) and precipitation (b) from April to August during the period 1980-2012. Note that the period from April to August corresponds to the carbon uptake period of most northern temperate and boreal stations. Regions with mean annual NDVI (AVHRR NDVI3 g dataset) less than 0.1 were masked.

Figure S6 Trends in monthly net CO_2 concentration change (MNCC) estimated by process-based models at Barrow, Alaska (BRW) during carbon uptake period (CUP) (a) and those during carbon release period (CRP) (b) from 1980 to 2012.

Figure S7 Spatial distribution of trends in net biome productivity (NBP) obtained from eight TRENDY models driven by rising CO_2 (a), climate change (b) and land use change (c) from April to August.

Figure S8 Trends in CO_2 seasonal peak-to-trough amplitude (AMP_{P-T}) estimated by eight TRENDY models and multi-model ensemble mean (MMEM) under different scenario simulations at northern temperate and boreal stations.

Figure S9 Same as Figure 2, but for trends in CO_2 seasonal trough-to-peak amplitude (AMP_{T-P}) (a) and trough-to-peak amplitude (AMP_{T-P}) (b) estimated by CLM4 model under nitrogen deposition scenarios at 26 northern temperate and boreal stations.

Figure S10 Trends in fossil fuel CO_2 emissions.

Figure S11 Spatial distribution of trends in net biome productivity (NBP) (a), gross primary productivity (GPP) (b) and total ecosystem respiration (TER) (c) from September to March for eight Trendy models driven by climate change only.

Figure S12 Same as Figure S5, but for trends in CO_2 seasonal trough-to-peak amplitude (AMP_{T-P}).

Figure S13 Spatial distribution of trends in net biome productivity (NBP) (a), gross primary productivity (GPP) (b) and total ecosystem respiration (TER) (c) from September to March for eight Trendy models driven by rising CO_2 only.

Figure legends

Figure 1 Observed and modeled trends in CO_2 seasonal peak-to-trough amplitude (AMP_{P-T}) (a) and trough-to-peak amplitude (AMP_{T-P}) (b) during 1980-2012. The modeled AMP_{P-T}/AMP_{T-P} trends were calculated based on eight TRENDY models and the multi-model ensemble mean (MMEM) in the T1 transport simulation (see methods). The abbreviated names of the 26 stations measuring atmospheric CO_2 concentrations in the northern temperate and boreal regions are shown at the top of the figure. The stations were sorted based on their latitudes, from 23 ℕ to 90 ℕ. Each row represents the trends for the various stations, and each column represents the trends derived from observation and the model simulations at a station. Gray grids indicate non-significant trends (P>0.10), colored grids without slashes indicate significant trends (P<0.05) and colored grids with slashes indicate marginally significant trends (P<0.10). The number in each grid is the value of the trend. Station abbreviations are defined in Table S1.

Figure 2 Trends in CO_2 seasonal peak-to-trough amplitude (AMP_{P-T}) (a) and trough-to-peak amplitude (AMP_{T-P}) (b) estimated by multi-model ensemble mean (MMEM) under various scenarios for the 26 northern temperate (23-50 ^{o}N) and boreal (north of 50 ^{o}N) stations. The results are presented based on the latitudes of the stations. The individual effects of changes in atmospheric CO_2 ('CO_2'), climate ('CLIM'), land use ('LU'), fossil fuel ('FF'), ocean-air carbon flux ('Ocean') and wind ('Wind') on the CO_2 seasonal amplitudes were derived from transport simulations (T2 - T6), (T3 - T2), (T4 - T3), (T7 - T6), (T8 - T6) and T6, respectively (see Methods and Table S4). Significant (P<0.05) trends for each scenario are denoted by two

dots, and marginally significant (P<0.10) trends are denoted by one dot, in the middle of the bars.

Figure 3 Trends in CO_2 seasonal peak-to-trough amplitude (AMP_{P-T}) (a) and trough-to-peak amplitude (AMP_{T-P}) (b) estimated by multi-model ensemble mean (MMEM) under different scenarios, averaged over the stations from the northern temperate (23-50^{o}N) and boreal (north of 50^{o}N) region. Model scenario simulations include changes in atmospheric CO_2 ('CO_2'), climate ('CLIM'), land use ('LU'), fossil fuel ('FF'), ocean-air carbon flux ('Ocean') and wind ('Wind'). Uncertainties are shown by error bars based on the standard deviation of AMP trends across the stations in each region.

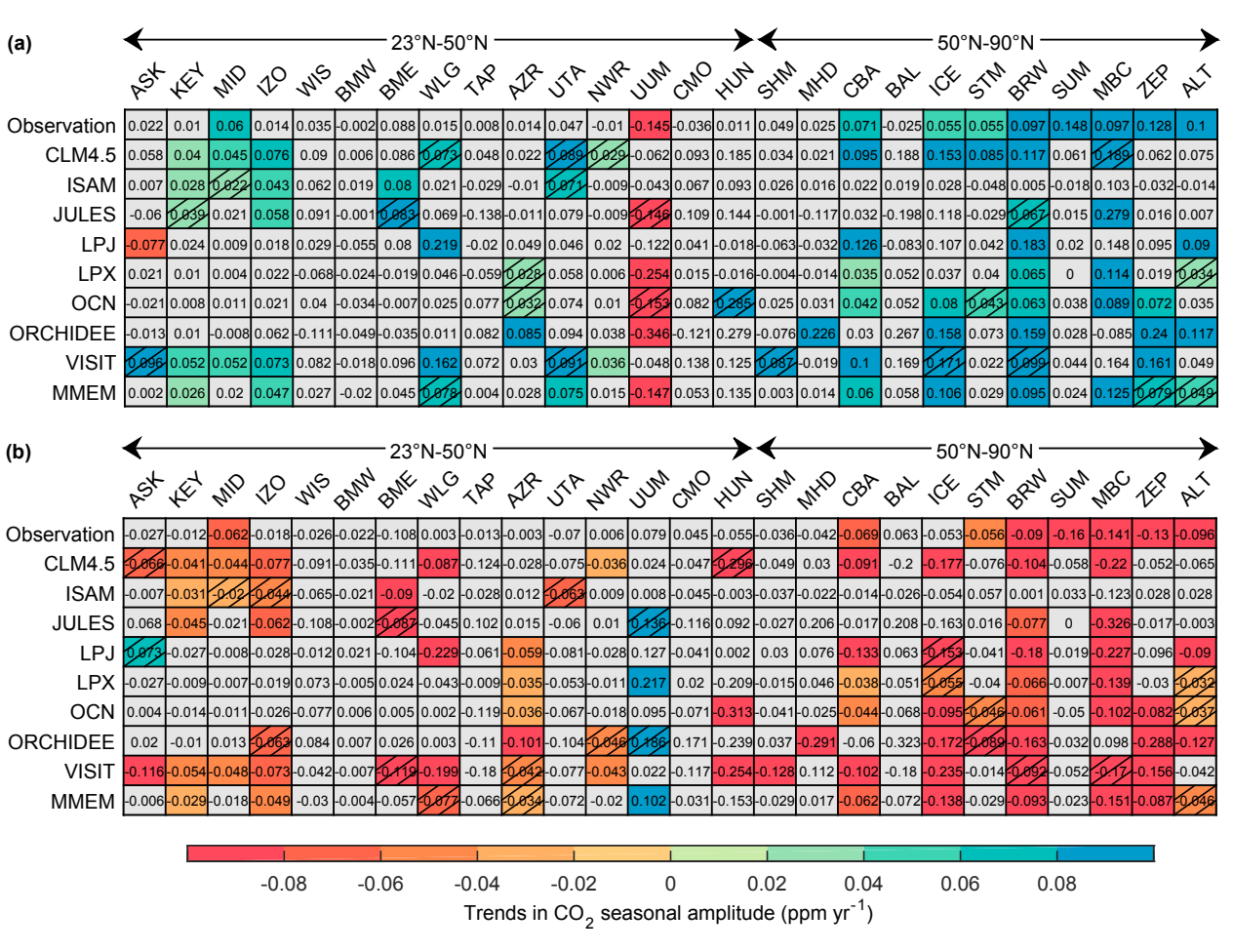
(a)
23°N-50°N
50°N-90°N
ASK KEY MID IZO WIS BMW BME WLG TAP AZR UTA NWR UUM CMO HUN SHM MHD CBA BAL ICE STM BRW SUM MBC ZEP ALT
Observation 0.022 0.01 0.06 0.014 0.035 -0.002 0.088 0.015 0.008 0.014 0.047 -0.01 -0.145 -0.036 0.011 0.049 0.025 0.071 -0.025 0.055 0.055 0.097 0.148 0.097 0.128 0.1
CLM4.5 0.058 0.04 0.045 0.076 0.09 0.006 0.086 0.073 0.048 0.022 0.089 0.029 -0.062 0.093 0.185 0.034 0.021 0.095 0.188 0.153 0.085 0.117 0.061 0.189 0.062 0.075
ISAM 0.007 0.028 0.022 0.043 0.062 0.019 0.08 0.021 -0.029 -0.01 0.071 -0.009 -0.043 0.067 0.093 0.026 0.016 0.022 0.019 0.028 -0.048 0.005 -0.018 0.103 -0.032 -0.014
JULES -0.06 0.039 0.021 0.058 0.091 -0.001 0.083 0.069 -0.138 -0.011 0.079 -0.009 0.146 0.109 0.144 -0.001 -0.117 0.032 -0.198 0.118 -0.029 0.067 0.015 0.279 0.016 0.007
LPJ -0.077 0.024 0.009 0.018 0.029 -0.055 0.08 0.219 -0.02 0.049 0.046 0.02 -0.122 0.041 -0.018 -0.063 -0.032 0.126 -0.083 0.107 0.042 0.183 0.02 0.148 0.095 0.09
LPX 0.021 0.01 0.004 0.022 -0.068 -0.024 -0.019 0.046 -0.059 0.028 0.058 0.006 -0.254 0.015 -0.016 -0.004 -0.014 0.035 0.052 0.037 0.04 0.065 0 0.114 0.019 0.034
OCN -0.021 0.008 0.011 0.021 0.04 -0.034 -0.007 0.025 0.077 0.032 0.074 0.01 -0.153 0.082 0.285 0.025 0.031 0.042 0.052 0.08 0.043 0.063 0.038 0.089 0.072 0.035
ORCHIDEE -0.013 0.01 -0.008 0.062 -0.111 -0.049 -0.035 0.011 0.082 0.085 0.094 0.038 -0.346 -0.121 0.279 -0.076 0.226 0.03 0.267 0.158 0.073 0.159 0.028 -0.085 0.24 0.117
VISIT 0.096 0.052 0.052 0.073 0.082 -0.018 0.096 0.162 0.072 0.03 0.091 0.036 -0.048 0.138 0.125 0.087 -0.019 0.1 0.169 0.171 0.022 0.099 0.044 0.164 0.161 0.049
MMEM 0.002 0.026 0.02 0.047 0.027 -0.02 0.045 0.078 0.004 0.028 0.075 0.015 -0.147 0.053 0.135 0.003 0.014 0.06 0.058 0.106 0.029 0.095 0.024 0.125 0.079 0.049
(b)
23°N-50°N
50°N-90°N
ASK KEY MID IZO WIS BMW BME WLG TAP AZR UTA NWR UUM CMO HUN SHM MHD CBA BAL ICE STM BRW SUM MBC ZEP ALT
Observation -0.027 -0.012 -0.062 -0.018 -0.026 -0.022 -0.108 0.003 -0.013 -0.003 -0.07 0.006 0.079 0.045 -0.055 -0.036 -0.042 -0.069 0.063 -0.053 -0.056 -0.09 -0.16 -0.141 -0.13 -0.096
CLM4.5 -0.066 -0.041 -0.044 -0.077 -0.091 -0.035 -0.111 -0.087 -0.124 -0.028 -0.075 -0.036 0.024 -0.047 -0.296 -0.049 0.03 -0.091 -0.2 -0.177 -0.076 -0.104 -0.058 -0.22 -0.052 -0.065
ISAM -0.007 -0.031 -0.02 -0.044 -0.065 -0.021 -0.09 -0.02 -0.028 0.012 -0.062 0.009 0.008 -0.045 -0.003 -0.037 -0.022 -0.014 -0.026 -0.054 0.057 0.001 0.033 -0.123 0.028 0.028
JULES 0.068 -0.045 -0.021 -0.062 -0.108 -0.002 -0.087 -0.045 0.102 0.015 -0.06 0.01 0.136 -0.116 0.092 -0.027 0.206 -0.017 0.208 -0.163 0.016 -0.077 0 -0.326 -0.017 -0.003
LPJ 0.073 -0.027 -0.008 -0.028 -0.012 0.021 -0.104 -0.229 -0.061 -0.059 -0.081 -0.028 0.127 -0.041 0.002 0.03 0.076 -0.133 0.063 -0.153 -0.041 -0.18 -0.019 -0.227 -0.096 -0.09
LPX -0.027 -0.009 -0.007 -0.019 0.073 -0.005 0.024 -0.043 -0.009 -0.035 -0.053 -0.011 0.217 0.02 -0.209 -0.015 0.046 -0.038 -0.051 -0.055 -0.04 -0.066 -0.007 -0.139 -0.03 -0.032
OCN 0.004 -0.014 -0.011 -0.026 -0.077 0.006 0.005 0.002 -0.119 -0.036 -0.067 -0.018 0.095 -0.071 -0.313 -0.041 -0.025 -0.044 -0.068 -0.095 -0.048 -0.061 -0.05 -0.102 -0.082 -0.037
ORCHIDEE 0.02 -0.01 0.013 -0.063 0.084 0.007 0.026 0.003 -0.11 -0.101 -0.104 -0.046 0.186 0.171 -0.239 0.037 -0.291 -0.06 -0.323 -0.172 -0.089 -0.163 -0.032 0.098 -0.288 -0.127
VISIT -0.116 -0.054 -0.048 -0.073 -0.042 -0.007 -0.119 -0.199 -0.18 -0.042 -0.077 -0.043 0.022 -0.117 -0.254 -0.128 0.112 -0.102 -0.18 -0.235 -0.014 -0.092 -0.052 -0.17 -0.156 -0.042
MMEM -0.006 -0.029 -0.018 -0.049 -0.03 -0.004 -0.057 -0.077 -0.066 -0.034 -0.072 -0.02 0.102 -0.031 -0.153 -0.029 0.017 -0.062 -0.072 -0.138 -0.029 -0.093 -0.023 -0.151 -0.087 -0.046
-0.08 -0.06 -0.04 -0.02 0 0.02 0.04 0.06 0.08
Trends in CO2 seasonal amplitude (ppm yr-1)

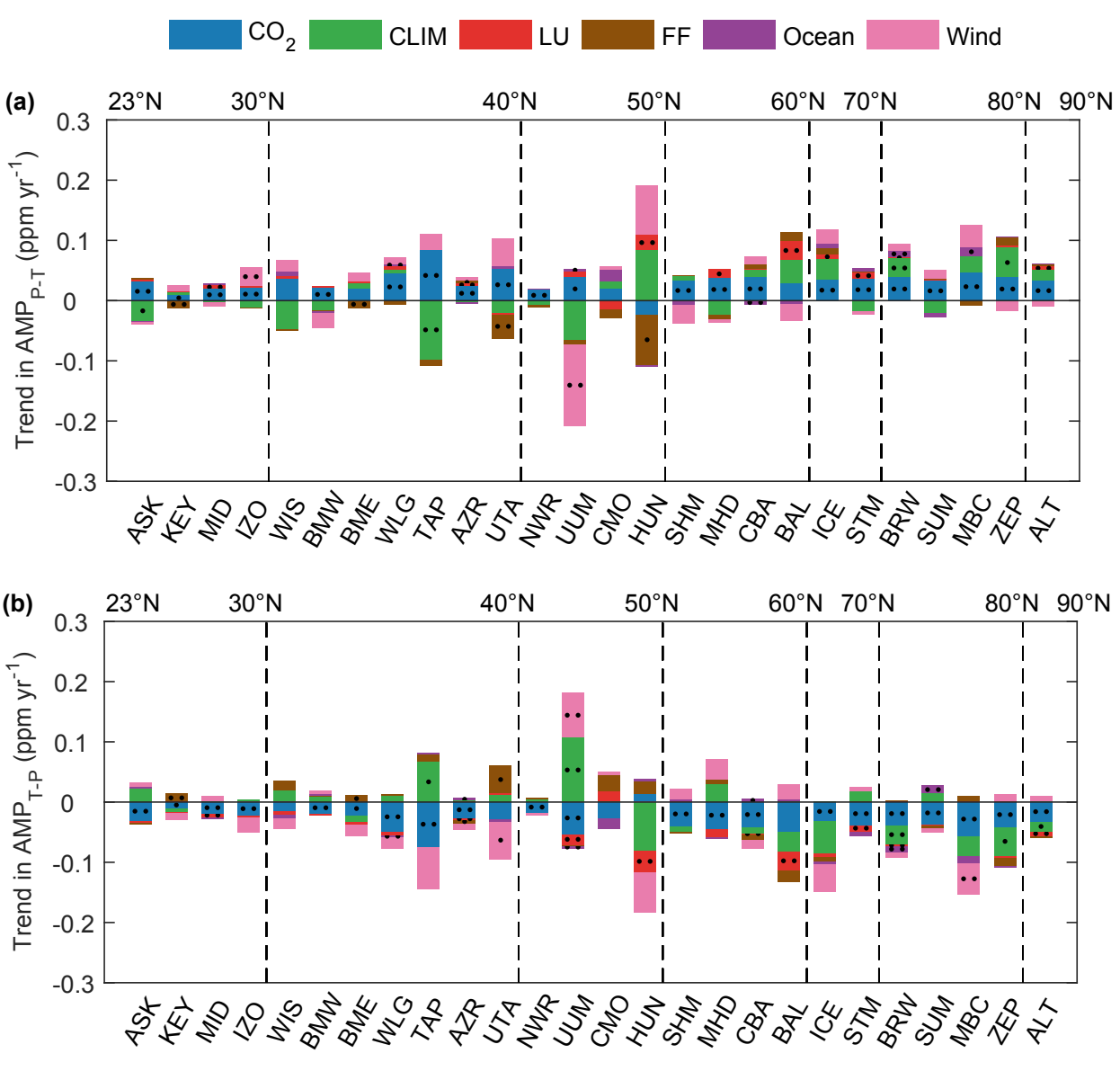
CO2
CLIM
LU
FF
Ocean
Wind
(a)
23°N
30°N
40°N
50°N
60°N
70°N
80°N
90°N
Trend in AMP P-T (ppm yr-1)
0.3
0.2
0.1
0
-0.1
-0.2
-0.3
ASK
KEY
MID
IZO
WIS
BMW
BME
WLG
TAP
AZR
UTA
NWR
UUM
CMO
HUN
SHM
MHD
CBA
BAL
ICE
STM
BRW
SUM
MBC
ZEP
ALT
(b)
Trend in AMP T-P (ppm yr-1)

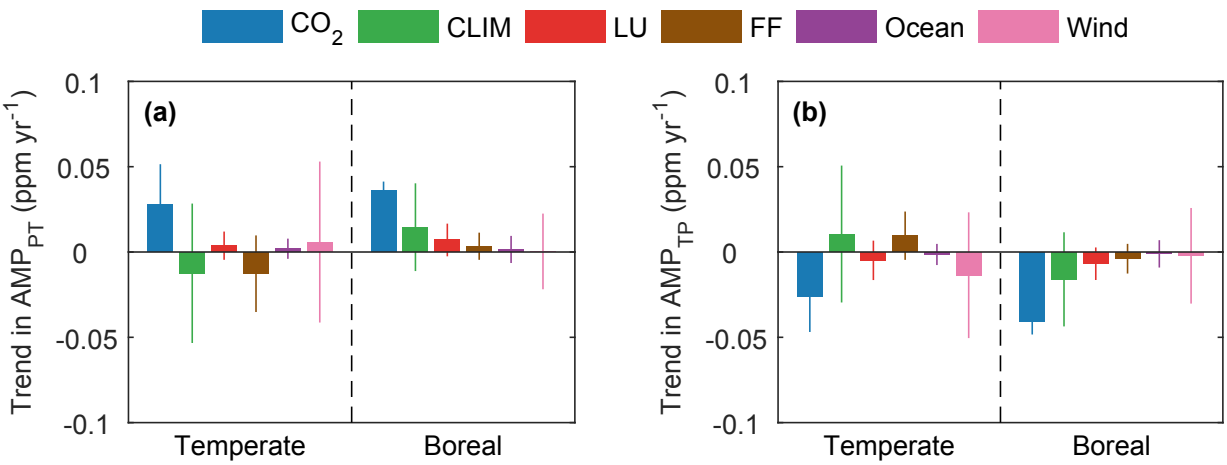
CO2
CLIM
LU
FF
Ocean
Wind
(a)
(b)
0.1
0.05
0
-0.05
-0.1
Trend in AMPPT (ppm yr-1)
Trend in AMPTP (ppm yr-1)
Temperate
Boreal

Table S1 Atmospheric CO_2 measurement stations (data coverage > 15 years in the period of 1980-2012) used in the study and estimated trends of peak-to-trough amplitude (AMP_{P-T}) and trough-to-peak amplitude (AMP_{T-P}). The 95% confidence intervals were calculated for each trend estimate.

Station name	abbreviation	Latitude (°N)	Longitude (°E)	Period	AMP_{P-T} (ppm yr^{-1})	AMP_{T-P} (ppm yr^{-1})
Alert, Nunavut	ALT	82.45	-62.52	1985-2012	0.100±0.036	-0.096±0.042
Ny-Alesund, Svalbard	ZEP	78.91	11.89	1994-2012	0.128±0.056	-0.130±0.076
Mould Bay, Northwest Territories	MBC	76.25	-119.35	1980-1997	0.097±0.090	-0.141±0.098
Summit	SUM	72.60	-38.42	1997-2012	0.148±0.111	-0.160±0.117
Barrow, Alaska	BRW	71.32	-156.60	1980-2012	0.097±0.032	-0.090±0.033
Ocean Station M	STM	66.00	2.00	1981-2009	0.055±0.024	-0.056±0.027
Storhofdi, Vestmannaeyjar	ICE	63.40	-20.29	1992-2012	0.055±0.053	-0.053±0.066
Baltic Sea	BAL	55.50	16.67	1992-2011	-0.025±0.323	0.063±0.319
Cold Bay, Alaska	CBA	55.20	-162.72	1980-2012	0.071±0.042	-0.069±0.043
Mace Head, County Galway	MHD	53.33	-9.90	1991-2012	0.025±0.076	-0.042±0.100
Shemya Island, Alaska	SHM	52.72	174.10	1985-2012	0.049±0.071	-0.036±0.070
Hegyhatsal	HUN	46.95	16.65	1993-2012	0.011±0.542	-0.055±0.573
Cape Meares, Oregon	CMO	45.48	-123.97	1982-1997	-0.036±0.190	0.045±0.205

Ulaan Uul	UUM	44.45	111.10	1992-2012	-0.145 ±0.141	0.079 ±0.136
Niwot Ridge, Colorado	NWR	40.05	-105.63	1980-2012	-0.010 ±0.046	0.006 ±0.045
Wendover, Utah	UTA	39.90	-113.72	1993-2012	0.047 ±0.143	-0.070 ±0.161
Terceira Island, Azores	AZR	38.75	-27.08	1980-2012	0.014 ±0.066	-0.003 ±0.045
Tae-ahn Peninsula	TAP	36.73	126.13	1990-2012	0.008 ±0.305	-0.013 ±0.272
Mt. Waliguan	WLG	36.27	100.92	1990-2012	0.015 ±0.106	0.003 ±0.116
St. Davids Head, Bermuda	BME	32.37	-64.65	1989-2010	0.088 ±0.123	-0.108 ±0.141
Tudor Hill, Bermuda	BMW	32.26	-64.88	1989-2012	-0.002 ±0.097	-0.022 ±0.102
WIS Station, Negev Desert	WIS	30.86	34.78	1995-2012	0.035 ±0.126	-0.026 ±0.173
Izana, Tenerife, Canary Islands	IZO	28.30	-16.48	1991-2012	0.014 ±0.049	-0.018 ±0.058
Sand Island, Midway	MID	28.22	-177.37	1985-2012	0.060 ±0.051	-0.062 ±0.055
Key Biscayne, Florida	KEY	25.67	-80.20	1980-2012	0.010 ±0.040	-0.012 ±0.039
Assekrem	ASK	23.26	5.63	1995-2012	0.022 ±0.038	-0.027 ±0.048

Table S2 Details of dynamic global vegetation models used in this study. Among the nine models, eight models (CLM4.5, ISAM, JULES, LPJ, LPX, OCN, ORCHIDEE and VISIT) are from the TRENDY project and performed three simulations (S1, S2 and S3) following the TRENDYv2 protocol. In simulation S1, only atmospheric CO_2 concentration was varied. In simulation S2, atmospheric CO_2 and climate were varied. In simulation S3, atmospheric CO_2, climate and land use were varied. Note that models differ in the representation of land use change processes (Table S3).

Model Name	Abbreviation	Spatial Resolution	Period	Reference
Community Land Model version 4.5	CLM4.5	1.25 °×0.9375 °	1860-2012	Oleson *et al.*, 2013
Integrated Science Assessment Model	ISAM	0.5 °× 0.5 °	1901-2012	Jain *et al.*, 2013
The Joint UK Land Environment Simulator	JULES	1.875 °×1.25 °	1860-2012	Clark *et al.*, 2011
Lund-Potsdam-Jena	LPJ	0.5 °× 0.5 °	1901-2012	Sitch *et al.*, 2003
Land Surface Processes and Exchanges	LPX	1 °× 1 °	1860-2012	Stocker *et al.*, 2013
ORCHIDEE-CN	OCN	1 °× 1 °	1901-2012	Zaehle & Friend, 2010
Organizing Carbon and Hydrology in Dynamic Ecosystems	ORCHIDEE	2 °× 2 °	1901-2012	Krinner *et al.*, 2005
Vegetation Integrative Simulator for Trace gases	VISIT	0.5 °× 0.5 °	1901-2012	Kato *et al.*, 2013
Community Land Model version 4.0	CLM4	0.5 °× 0.5 °	1850-2012	Oleson *et al.*, 2010; Mao *et al.*, 2013

Table S3 Processes of land use change and management considered in TRENDYv2 models (Le Quéré *et al.*, 2014).

	CLM4.5	ISAM	JULES	LPJ	LPX	OCN	ORCHIDEE	VISIT
Deforestation and forest regrowth after abandonment	√	√	√	√	√	√	√	√
Wood harvest and forest degradation	√	√						√
Shifting cultivation	√							√
Cropland harvest	√				√	√	√	√
Peat fires	√							
Fire simulation and/or suppression	√			√	√			√

Table S4 Summary of transport simulations performed. We use 9 dynamic global vegetation models (see Table S2) to simulate land-atmosphere CO_2 exchange (NEE), 1 model to simulate ocean-atmosphere CO_2 exchange and gridded monthly fossil fuel CO_2 emission from CDIAC. Then LMDZ4, a 3D atmospheric tracer transport model, is performed to transport carbon flux into a point estimate of CO_2 concentration at each observation station. The land-atmosphere CO_2 exchange is varying in transport simulations T1~T5 but constant at 1979 value in T6~T8. Among these eight transport simulations, T1 indicates the effect of all factors, while T6 indicates the effect of wind. The effects of CO_2 fertilization, climate change, land use change, nitrogen deposition, fossil fuel and ocean flux are estimated from (T2-T6), (T3-T2), (T4-T3), T5, (T7-T6) and (T8-T6), respectively. Note that in transport simulations T1~T4 and T6~T8, land-atmosphere CO_2 exchange was derived from eight TRENDYv2 models; in transport simulation T5, land-atmosphere CO_2 exchange was derived from CLM4 model only (Table S2).

Transport Simulation	**Land-atmosphere CO_2 exchange**				**Fossil fuel**	**Ocean-atmosphere CO_2 exchange**	**Wind**
	CO_2	**Climate**		**Nitrogen deposition**			
T1	vary	vary	vary	-	vary	vary	vary
T2	vary	constant	constant	-	constant	constant	vary
T3	vary	vary	constant	-	constant	constant	vary
T4	vary	vary	vary	-	constant	constant	vary
T5	constant	constant	constant	vary	constant	constant	constant
T6	constant	constant	constant	-	constant	constant	vary
T7	constant	constant	constant	-	vary	constant	vary
T8	constant	constant	constant	-	constant	vary	vary

Figure S1 Spatial distribution of the NOAA-ERSL stations (data coverage > 15 years) used in this study. Stations in northern temperate region (23-50 ℃N) and boreal region (north of 50 ℃N) are shown in red and blue, respectively. Station abbreviations are defined in Table S1.

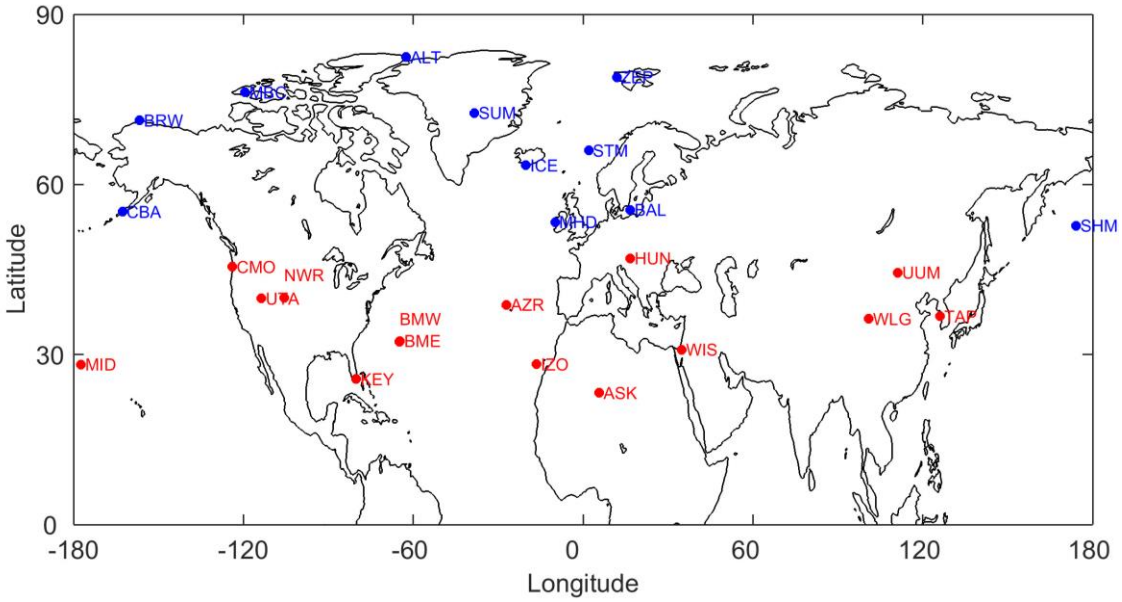

Figure S2 A schematic describing the terms we used to characterize the seasonal amplitude of atmospheric CO_2. In this example, we show the detrended seasonal cycle of CO_2 at Barrow, Alaska (BRW, 71°N) during 1980-1981. The peak (maximum) value and the trough (minimum) value of CO_2 cycle in each year are marked in blue and red circle, respectively. We divided CO_2 amplitude into peak-to-trough (AMP_{P-T}) and trough-to-peak (AMP_{T-P}). AMP_{P-T} was calculated as the difference between the peak value and the trough value of CO_2 seasonal cycle in a year (blue line), while AMP_{T-P} was calculated as the difference between the trough value of CO_2 seasonal cycle in a year and the peak value of the cycle in the next year (red line). The AMP_{P-T} and AMP_{T-P} represent seasonal variation in atmospheric CO_2 concentration during the net carbon uptake period (marked in light gray) and the net carbon release period (marked in dark gray), respectively. Note that the sign convention is positive for AMP_{P-T} and negative for AMP_{T-P}.

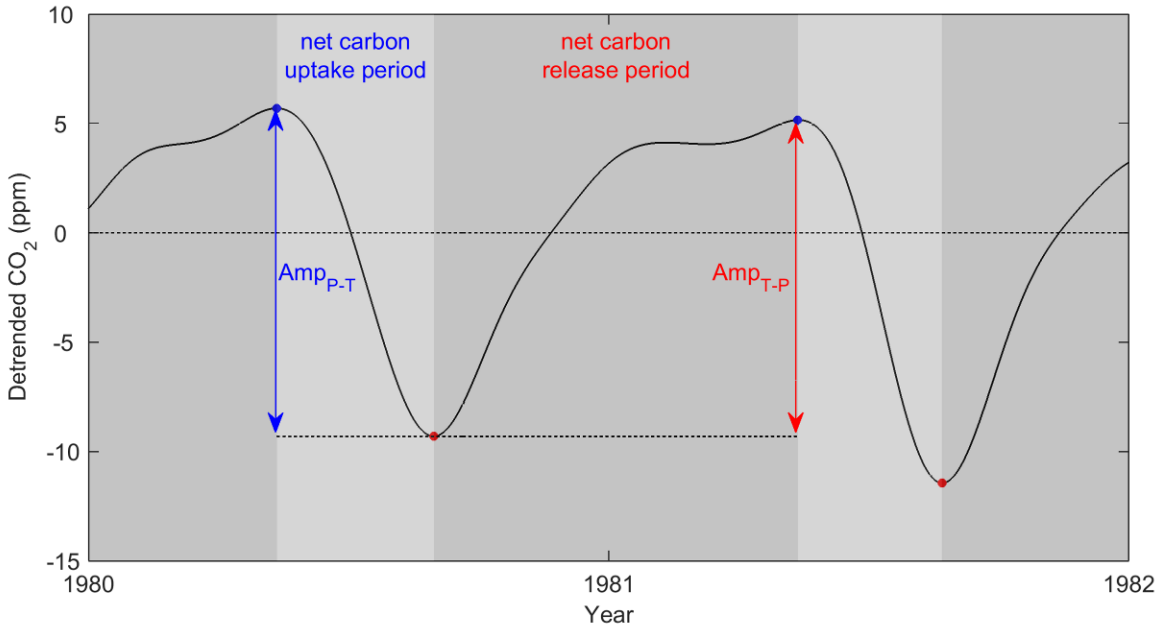

Figure S3 Observed trends in monthly net CO_2 concentration change (MNCC) from long-term records of the global NOAA-ERSL surface flask air-sampling network. Here the monthly net CO_2 concentration change (MNCC) was calculated as the difference between the detrended CO_2 value in the first week of a given month and that of next month. Shown on the top of the figure are the abbreviated names of 26 atmospheric CO_2 concentration measurement stations in northern temperate and boreal regions. We sort the stations according to their latitudes, from 23 ℕ to 90 ℕ. Each row represents trends in MNCC for a certain month at different stations, while each column represents trends in MNCC for different months at a certain station. Gray grids show insignificant trends ($P > 0.10$), while colored grids without slashes indicate statistically significant ($P < 0.05$) and those with slashes marginal significant ($P < 0.10$). The number in each grid shows the value of the trend. Station abbreviations are defined in Table S1.

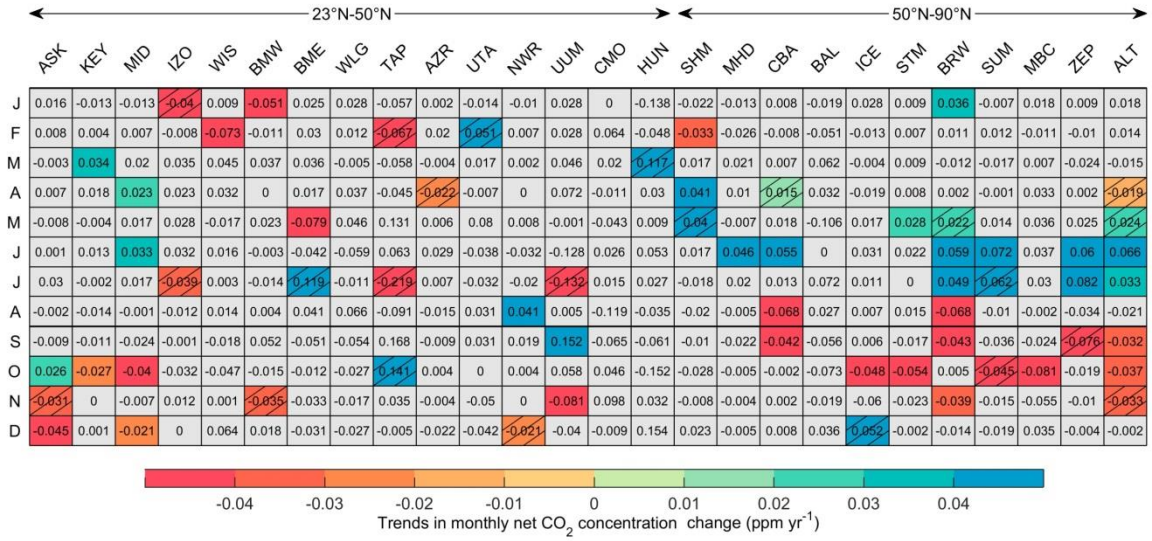

Figure S4 Observed and modeled trends in CO_2 seasonal peak-to-trough amplitude (AMP_{P-T}) (a, c) and trough-to-peak amplitude (AMP_{T-P}) (b, d) during 1980 to 2012, averaged over the stations from northern temperate region (23-50ºN) and boreal region (north of 50ºN). In (a) and (b), all stations in northern temperate and boreal region are included. In (c) and (d), only stations with observed significant AMP trends are taken into account. Here the modeled trends were calculated based on eight TRENDY models under T1 transport simulation (see methods). We also calculated the multi-model ensemble mean (MMEM) trends. Uncertainties are shown by error bars based on the standard deviation of AMP trends across stations in each region.

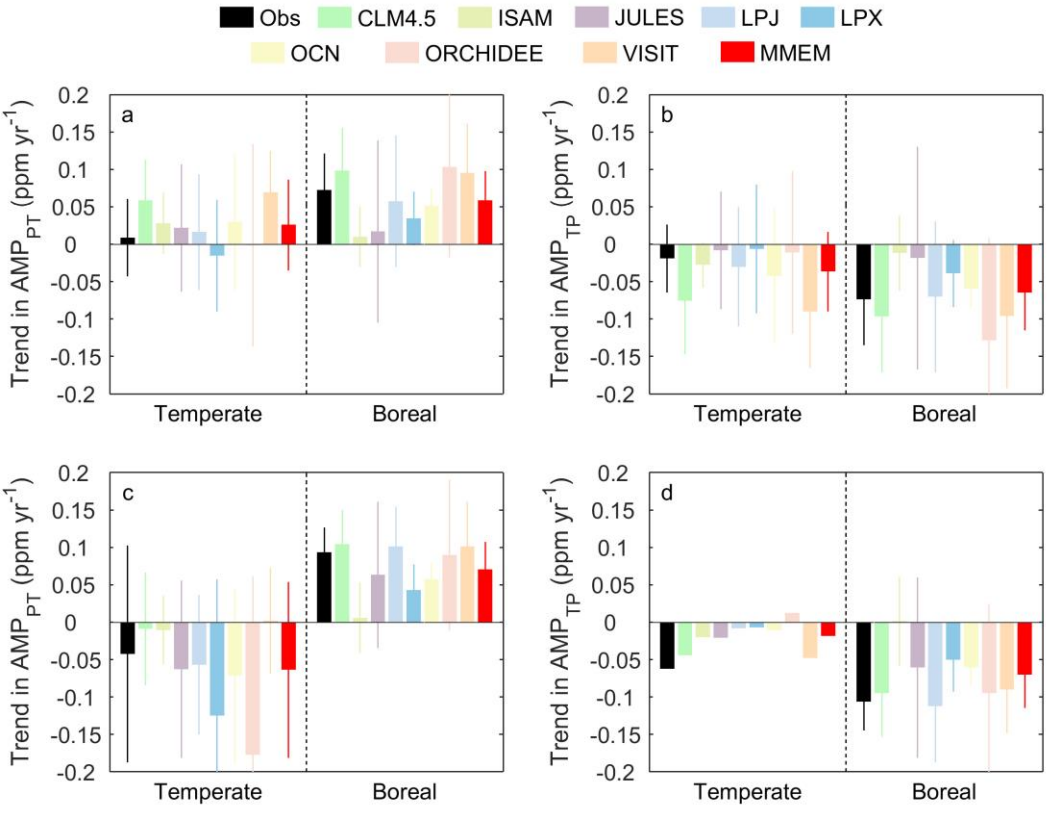

Figure S5 Spatial distribution of trends in temperature (a) and precipitation (b) from April to August during the period 1980-2012. Note that the period from April to August corresponds to the carbon uptake period of most northern temperate and boreal stations. Regions with mean annual NDVI (AVHRR NDVI3 g dataset) less than 0.1 were masked.

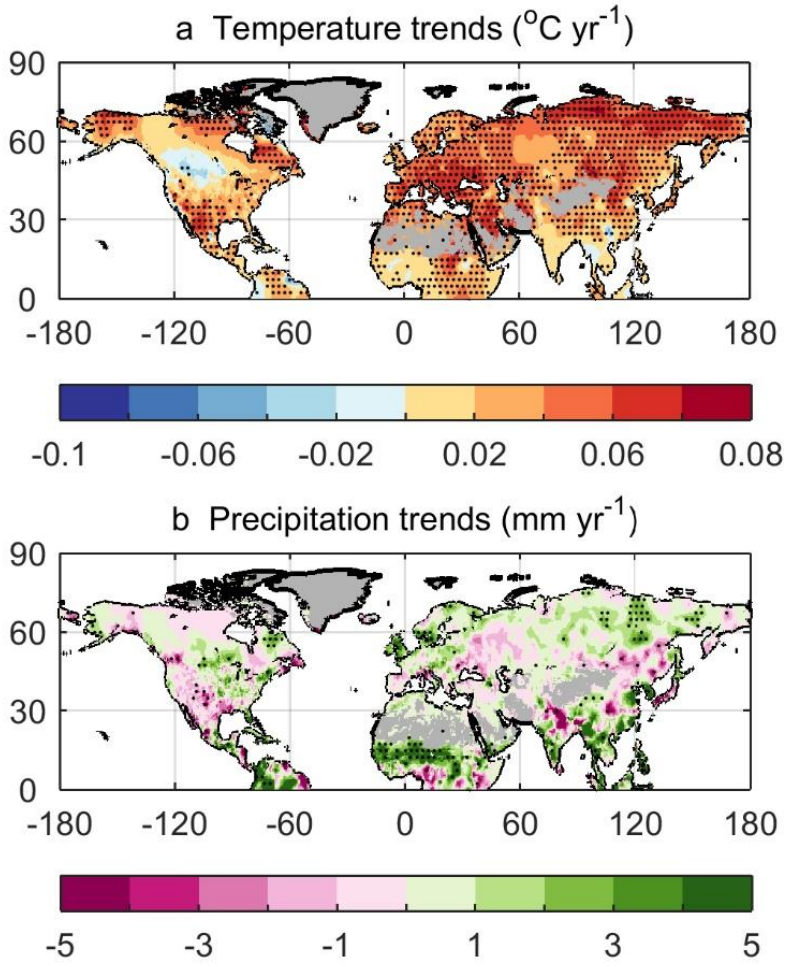

Figure S6 Trends in monthly net CO_2 concentration change (MNCC) estimated by process-based models at Barrow, Alaska (BRW) during carbon uptake period (CUP) (a) and those during carbon release period (CRP) (b) from 1980 to 2012. Model scenario simulations include change in atmospheric CO_2 ('CO_2'), climate ('CLIM'), land use ('LU'), fossil fuel ('FF'), ocean-air carbon flux ('Ocean'), wind ('Wind') and nitrogen deposition ('NDEP'). For a certain scenario simulation (except "NDEP"), the different colored bars show the trends in MNCC of different months derived from multi-model ensemble mean (MMEM). For 'NDEP' scenario, the different colored bars show results from CLM4 model only. The vertical solid lines indicate the maximum and minimum trends across models. We also calculated the total monthly trends during CUP (CRP) and denote them with horizontal black solid lines. Note that the carbon uptake period (CUP) at BRW station refers to the period from May to August during which positive values of MNCC are detected. Similarly, carbon release period (CRP) refers to the period from September to April during which negative values of MNCC are obtained.

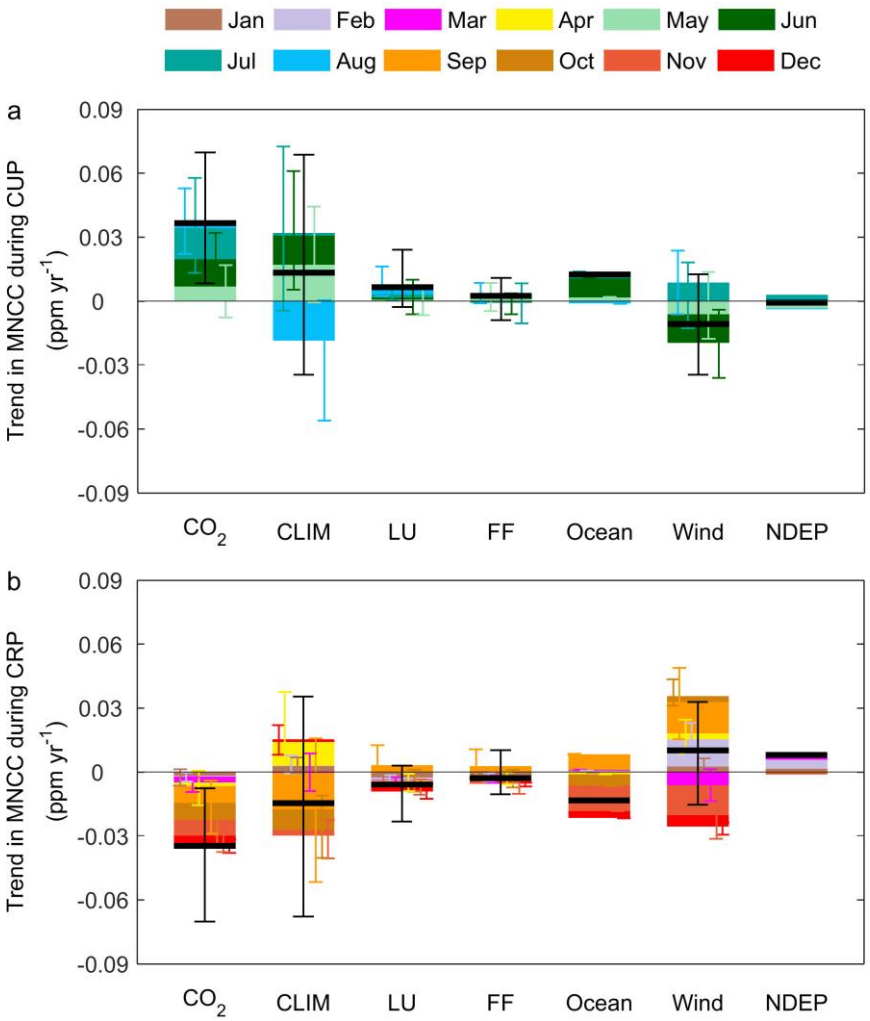

Figure S7 Spatial distribution of trends in net biome productivity (NBP) obtained from eight TRENDY models driven by rising CO_2 (a), climate change (b) and land use change (c) from April to August. Note that the period from April to August corresponds to the carbon uptake period of most northern temperate and boreal stations. Regions with mean annual NDVI (AVHRR NDVI3 g dataset) less than 0.1 were masked. The study period is from 1980 to 2012.

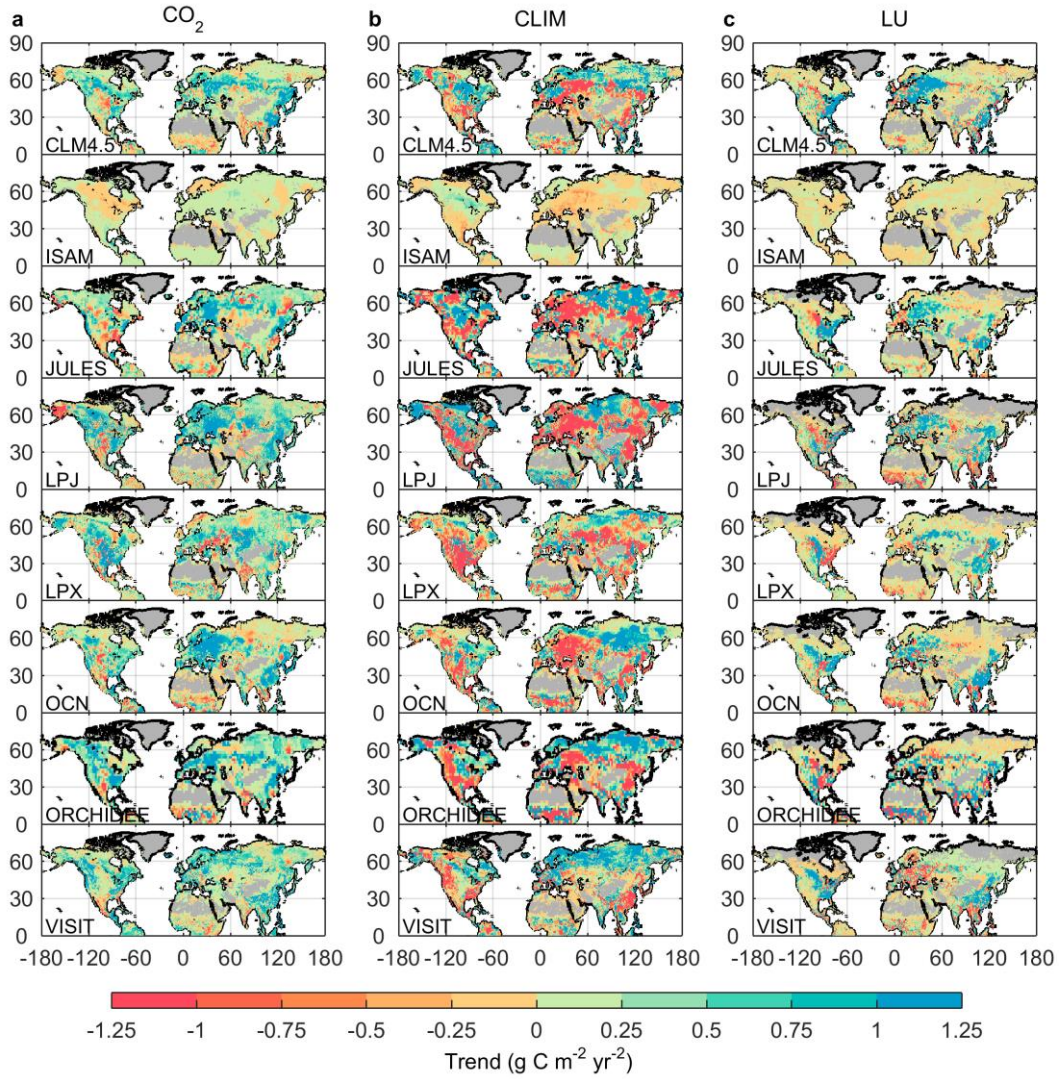

Figure S8 Trends in CO_2 seasonal peak-to-trough amplitude (AMP_{P-T}) estimated by eight TRENDY models and multi-model ensemble mean (MMEM) under different scenario simulations at northern temperate and boreal stations. The scenario simulations include 'CO_2' (a), 'CLIM' (b), 'LU' (c), 'Fossil fuel' (d), 'Ocean' (e) and 'Wind' (f) (Table S4). Gray grids show insignificant trends (P > 0.10), while colored grids without slashes indicate statistically significant (P < 0.05) and those with slashes marginal significant (P < 0.10). The number in each grid shows the value of the trend. Station abbreviations are defined in Table S1.

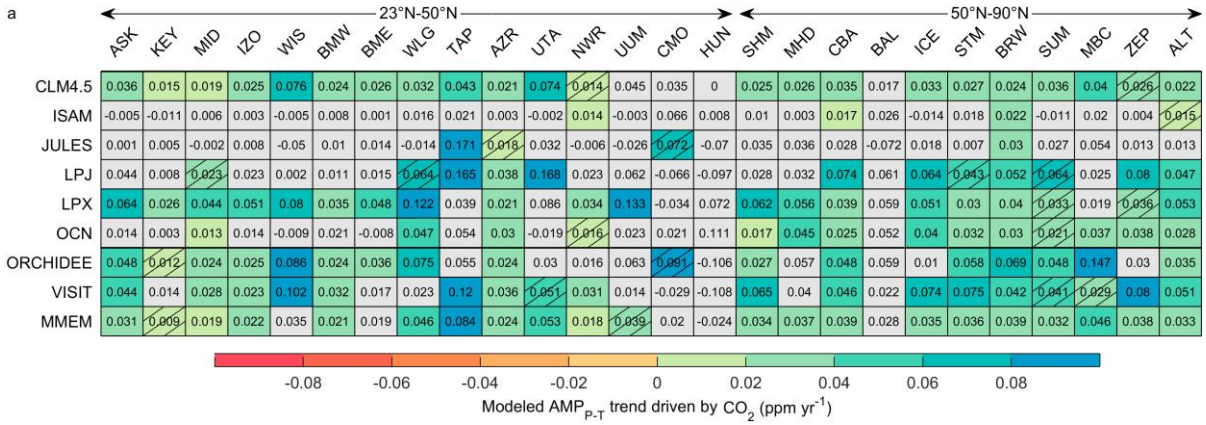

d

	23°N-50°N														50°N-90°N										
	ASK	KEY	MID	IZO	WIS	BMW	BME	WLG	TAP	AZR	UTA	NWR	UUM	CMO	HUN	SHM	MHD	CBA	BAL	ICE	STM	BRW	SUM	MBC	ZEP	ALT
CLM4.5	-0.005	-0.015	-0.005	-0.008	0.01	-0.002	-0.025	0.001	-0.01	0.005	0.005	0.006	-0.001	-0.014	-0.079	-0.014	-0.007	0.007	0.009	-0.001	0.007	-0.002	-0.009	-0.006	-0.002	0
ISAM	0.003	-0.01	-0.001	-0.006	-0.012	0.002	-0.003	-0.008	-0.062	0	-0.019	0.006	-0.017	0.023	-0.059	-0.007	-0.024	-0.012	0.022	-0.004	0.003	-0.021	0.012	0.008	0.013	0.002
JULES	0.003	-0.022	-0.012	-0.001	-0.043	0.012	-0.044	-0.02	-0.019	0.027	-0.022	-0.006	-0.039	-0.012	-0.083	0.027	0.024	0.002	0.015	0.031	0	-0.011	0.009	-0.056	0.03	0.012
LPJ	-0.01	-0.036	0	-0.006	-0.02	-0.014	-0.022	-0.036	0.022	0.007	-0.146	-0.016	-0.033	-0.02	-0.14	-0.017	-0.009	0.045	0.019	0.023	0.004	0.012	-0.006	-0.038	0.027	0.006
LPX	0.018	-0.001	0.002	0.005	-0.011	0.001	-0.01	-0.019	-0.006	0.002	-0.005	-0.003	0.06	-0.057	-0.078	0.002	-0.005	0.003	-0.005	0.005	0.003	0.008	-0.001	0.01	-0.006	0.002
OCN	0.002	-0.016	0	-0.016	0.035	-0.005	-0.017	0.004	-0.053	0.002	-0.041	-0.011	-0.026	0.009	0.005	0	-0.011	0	0.002	0.005	-0.006	0.004	0.001	0.007	0.017	-0.001
ORCHIDEE	0.009	0.017	0.002	0.007	-0.006	0.001	0.008	0.004	0.016	-0.005	-0.063	-0.009	-0.008	-0.03	-0.13	0	-0.01	0.007	0.064	-0.002	0.009	0.012	0.005	0.002	0.023	0.01
VISIT	0.006	-0.016	0.009	0.006	0.019	-0.018	0.015	0.025	0.028	0.001	-0.028	0.007	0.009	-0.025	-0.096	0.023	-0.021	0.004	-0.006	0.026	-0.005	-0.002	-0.003	0.009	-0.001	-0.004
MMEM	0.003	-0.013	-0.001	-0.002	-0.004	-0.003	-0.012	-0.006	-0.011	0.005	-0.04	-0.003	-0.007	-0.016	-0.082	0.002	-0.008	0.007	0.015	0.01	0.002	0	0.001	-0.008	0.013	0.003

Modeled AMP_{P-T} trend driven by Fossil fuel (ppm yr^{-1})

e

	23°N-50°N														50°N-90°N										
	ASK	KEY	MID	IZO	WIS	BMW	BME	WLG	TAP	AZR	UTA	NWR	UUM	CMO	HUN	SHM	MHD	CBA	BAL	ICE	STM	BRW	SUM	MBC	ZEP	ALT
CLM4.5	-0.002	-0.001	0.002	0	0.008	-0.002	0	0.003	0	-0.002	0.004	0	0.004	0.018	-0.003	-0.006	-0.001	-0.006	-0.004	0.01	0.005	0.01	-0.008	0.015	0.001	0.002
ISAM	-0.002	-0.001	0.003	0	0.007	-0.001	0	0.003	-0.001	-0.002	0.005	0	0.004	0.019	-0.003	-0.005	-0.001	-0.006	-0.005	0.007	0.005	0.01	-0.008	0.015	0.001	0.002
JULES	-0.002	-0.001	0.002	0	0.007	-0.002	0	0.003	0	-0.003	0.005	0	0.003	0.019	-0.003	-0.006	-0.001	-0.007	-0.004	0.008	0.005	0.01	-0.006	0.016	0.001	0.002
LPJ	-0.002	-0.001	0.003	0	0.008	-0.002	0	0.003	0	-0.002	0.004	0	0.004	0.018	-0.003	-0.005	-0.001	-0.006	-0.005	0.008	0.005	0.01	-0.007	0.014	0.002	0.002
LPX	-0.002	-0.001	0.003	0	0.007	-0.002	0	0.003	-0.001	-0.003	0.004	0	0.004	0.02	-0.003	-0.006	0	-0.006	-0.005	0.01	0.005	0.01	-0.008	0.015	0.001	0.002
OCN	-0.002	-0.001	0.003	0	0.007	-0.002	-0.001	0.003	-0.001	-0.003	0.004	0	0.004	0.019	-0.003	-0.006	-0.001	-0.006	-0.006	0.009	0.005	0.01	-0.008	0.015	0	0.002
ORCHIDEE	-0.002	-0.001	0.003	0	0.007	-0.002	0	0.003	-0.001	-0.003	0.005	0	0.004	0.017	-0.003	-0.006	-0.001	-0.006	-0.005	0.008	0.005	0.01	-0.008	0.015	0.002	0.002
VISIT	-0.001	-0.001	0.003	0	0.007	-0.002	-0.001	0.003	0	-0.003	0.004	0	0.004	0.019	-0.003	-0.004	-0.001	-0.006	-0.005	0.008	0.005	0.01	-0.008	0.015	0.002	0.002
MMEM	-0.002	-0.001	0.003	0	0.007	-0.002	0	0.003	0	-0.003	0.004	0	0.004	0.019	-0.003	-0.005	-0.001	-0.006	-0.005	0.008	0.005	0.01	-0.008	0.015	0.001	0.002

Modeled AMP_{P-T} trend driven by Ocean (ppm yr^{-1})

f

	23°N-50°N														50°N-90°N										
	ASK	KEY	MID	IZO	WIS	BMW	BME	WLG	TAP	AZR	UTA	NWR	UUM	CMO	HUN	SHM	MHD	CBA	BAL	ICE	STM	BRW	SUM	MBC	ZEP	ALT
CLM4.5	0.028	0.016	-0.003	0.043	0.031	-0.033	0.042	0.018	-0.051	-0.014	0.031	-0.01	-0.181	-0.001	0.009	-0.017	-0.059	0.028	-0.015	0.033	0	0.027	0.036	0.121	-0.039	-0.01
ISAM	0.015	0.027	0.015	0.043	0.066	0.011	0.064	0.015	0.04	-0.013	0.04	-0.021	-0.038	0.013	0.159	0.018	0.028	0.036	-0.027	0.024	-0.029	0.031	-0.021	0.073	-0.051	-0.014
JULES	-0.052	0.039	0.024	0.046	0.115	0.033	0.086	0.021	0.042	-0.039	0.022	-0.026	0.008	0.018	0.229	0.036	0.01	-0.019	-0.041	0.046	-0.018	0.008	-0.008	0.122	-0.057	-0.026
LPJ	-0.025	0.008	-0.001	0.029	0.063	-0.045	0.058	0.084	0.004	0.02	0.088	0.026	-0.085	-0.019	0.082	-0.062	-0.001	0.064	-0.097	0.007	0.015	0.024	0.056	0.038	-0.017	-0.011
LPX	0.027	-0.004	-0.009	0.02	-0.039	-0.016	-0.02	-0.017	-0.011	0.017	0.045	0.005	-0.205	0.027	-0.012	-0.035	0.016	0.002	0.005	0.008	-0.009	0.004	0.027	0.025	-0.002	0.001
OCN	-0.039	0.003	-0.023	0.023	-0.022	-0.03	-0.03	-0.005	0.121	0.02	0.044	0.001	-0.151	0.015	0.043	-0.022	0.004	0.016	0.015	0.017	-0.001	0	0.009	0.009	0	-0.008
ORCHIDEE	-0.03	-0.031	-0.055	0.015	-0.099	-0.088	-0.106	-0.101	0.047	0.067	0.061	0.028	-0.324	-0.114	0.159	-0.142	-0.002	-0.042	-0.086	0.029	-0.012	-0.008	0.023	-0.142	0.026	0
VISIT	0.047	0.034	-0.005	0.036	0.044	-0.036	0.024	0.078	0.021	-0.004	0.043	0.005	-0.114	0.113	-0.007	-0.026	-0.041	0.024	0.014	0.018	0.008	0.012	-0.003	0.054	0.009	-0.005
MMEM	-0.003	0.011	-0.007	0.032	0.02	-0.026	0.015	0.011	0.027	0.007	0.047	0.001	-0.136	0.007	0.083	-0.031	-0.006	0.014	-0.029	0.023	-0.006	0.012	0.015	0.037	-0.016	-0.009

Modeled AMP_{P-T} trend driven by Wind (ppm yr^{-1})

Figure S9 Same as Figure 2, but for trends in CO_2 seasonal trough-to-peak amplitude (AMP_{T-P}) (a) and trough-to-peak amplitude (AMP_{T-P}) (b) estimated by CLM4 model under nitrogen deposition scenarios at 26 northern temperate and boreal stations.

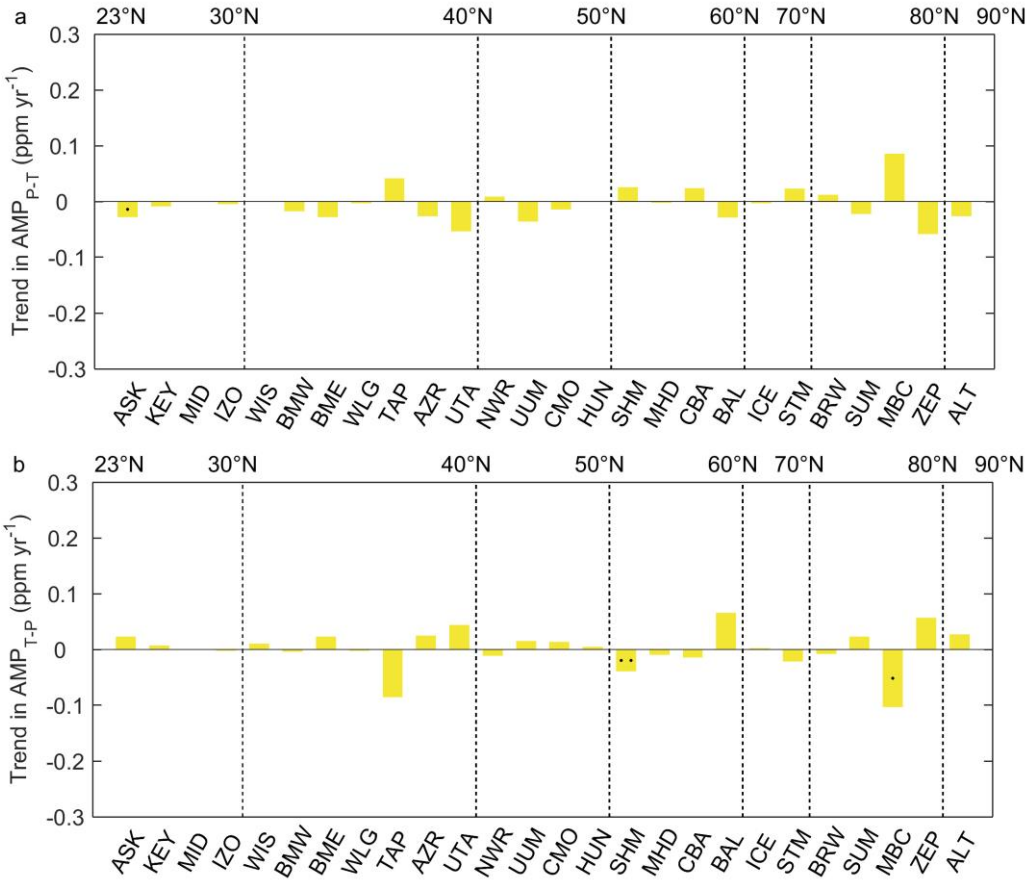

Figure S10 Trends in fossil fuel CO_2 emissions. (a) Time series of annual fossil fuel CO_2 emissions over global area, northern temperate area (23°N-50°N) and boreal area (north of 50°N) during 1980-2012. The slope of the trend and P values for different regions are denoted in different colors. (b) Spatial distribution of trends in fossil fuel CO_2 emissions from April to August. (c) Spatial distribution of trends in fossil fuel CO_2 emissions from September to March. Note that the months from April to August corresponds to the period calculating AMP_{P-T} for most northern temperate and boreal stations, while September to March corresponds to the period calculating AMP_{T-P}.

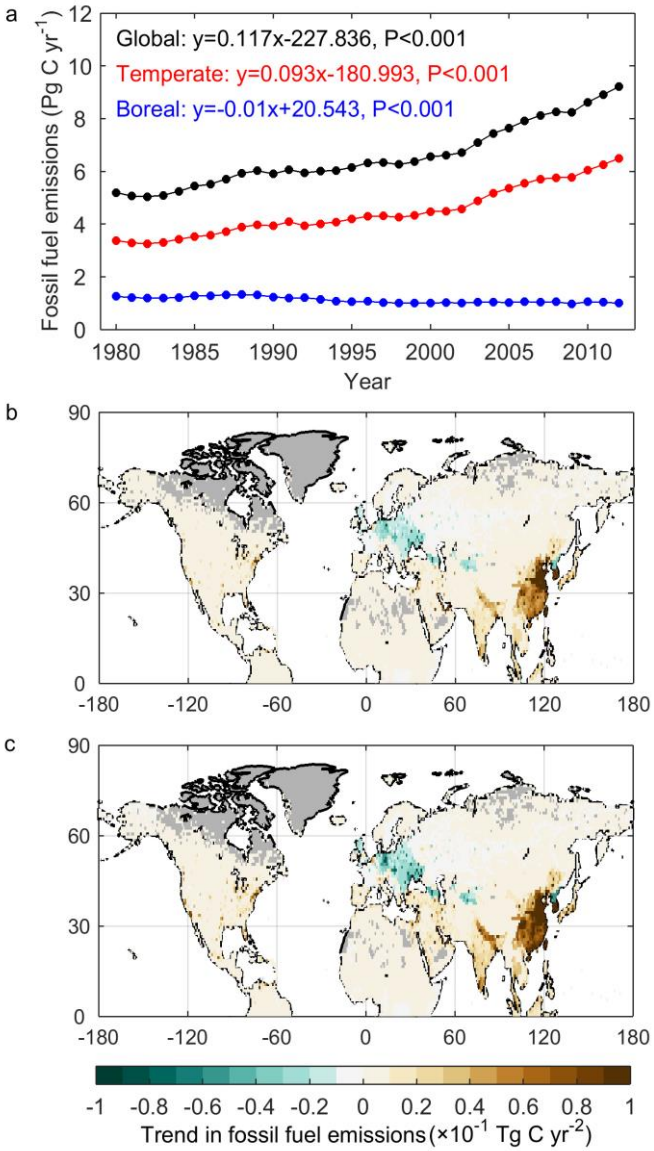

Figure S11 Spatial distribution of trends in net biome productivity (NBP) (a), gross primary productivity (GPP) (b) and total ecosystem respiration (TER) (c) from September to March for eight Trendy models driven by climate change only. Note that the period from September to March corresponds to the carbon release period (CRP) of most northern temperate and boreal stations. Regions with mean annual NDVI (AVHRR NDVI3 g dataset) less than 0.1 were masked. The study period is from 1980 to 2012.

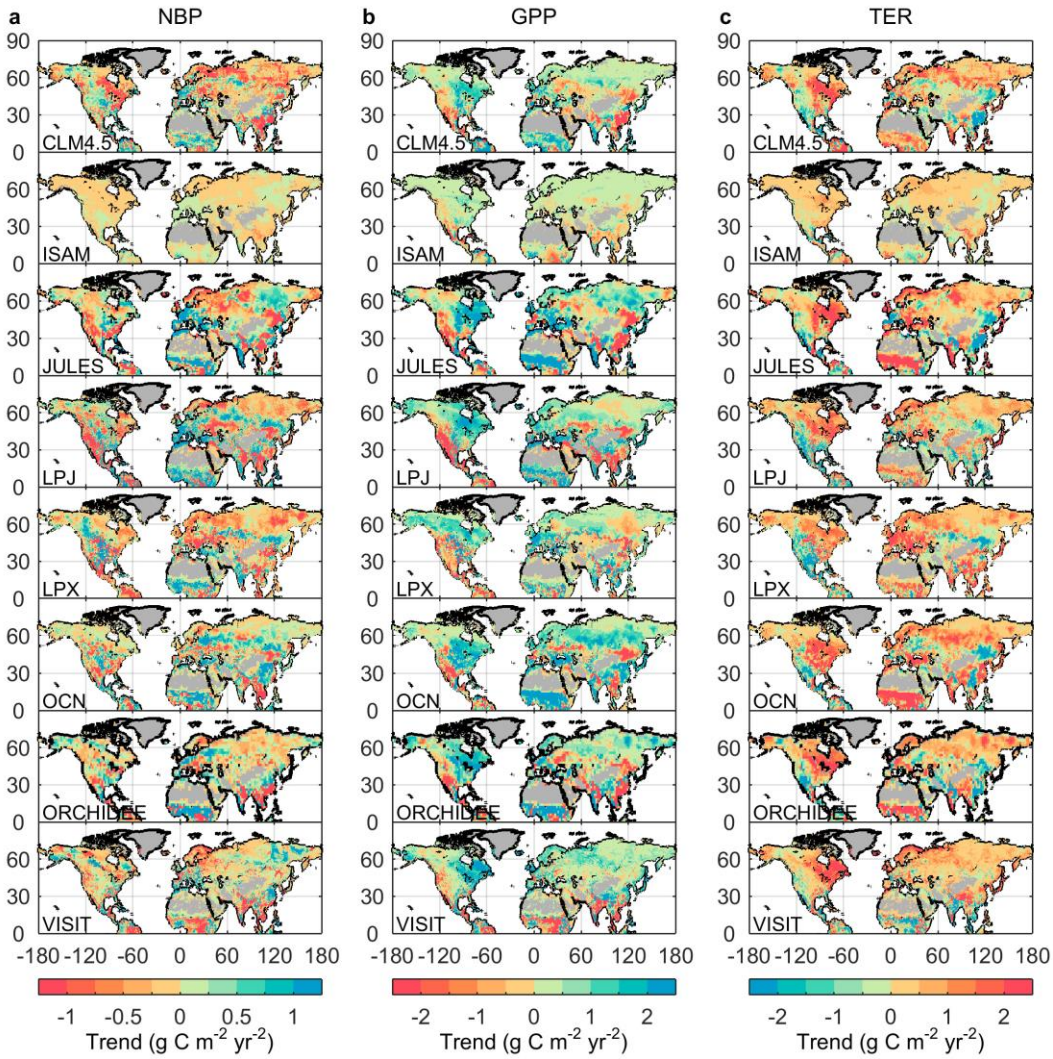

Figure S12 Same as Figure S8, but for trends in CO_2 seasonal trough-to-peak amplitude (AMP_{T-P}).

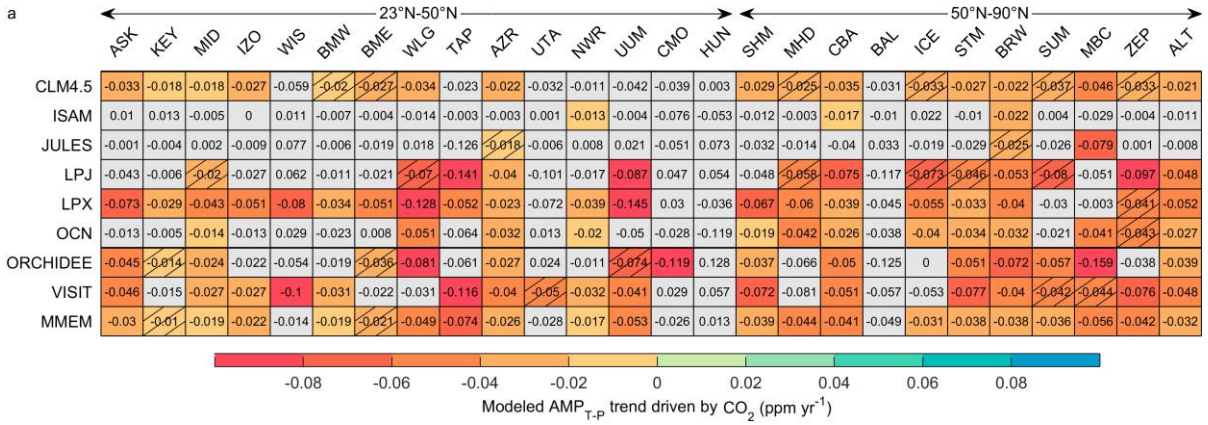

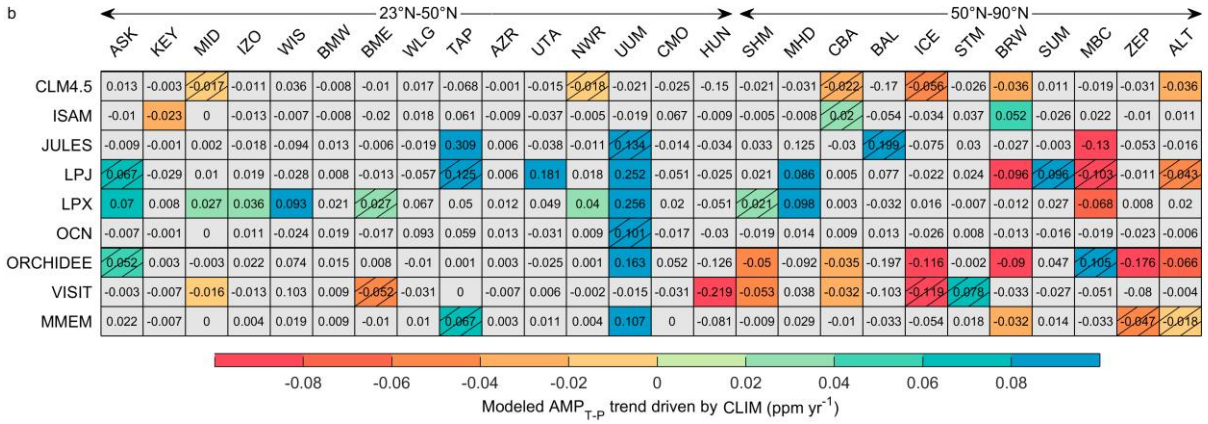

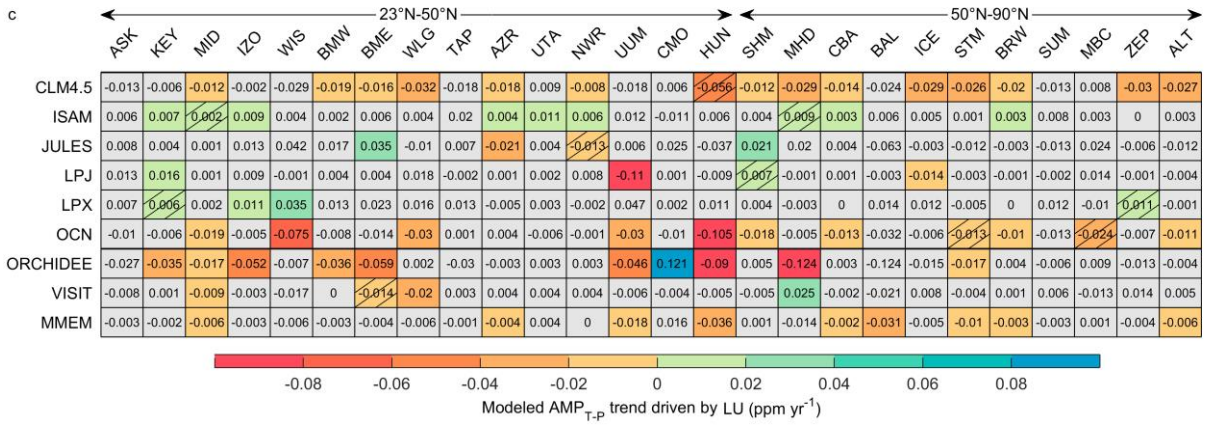

d

	ASK	KEY	MID	IZO	WIS	BMW	BME	WLG	TAP	AZR	UTA	NWR	UUM	CMO	HUN	SHM	MHD	CBA	BAL	ICE	STM	BRW	SUM	MBC	ZEP	ALT
	23°N-50°N															50°N-90°N										
CLM4.5	0.001	0.014	0.005	0.005	0.001	-0.001	0.027	-0.004	0.023	-0.005	0.003	-0.005	0.006	0.02	0.061	0.012	0.004	-0.007	-0.012	0.011	-0.008	0.004	0.007	0.012	0.006	-0.002
ISAM	-0.004	0.012	0.001	0.004	0.012	-0.007	0.001	0.006	0.071	-0.002	0.019	-0.008	-0.006	-0.025	-0.087	0.005	0.04	0.01	-0.018	0.009	-0.004	0.019	-0.014	-0.003	-0.014	-0.003
JULES	-0.009	0.029	0.012	-0.001	0.038	-0.014	0.049	0.014	0.066	-0.026	0.028	0.005	0	0.046	-0.038	-0.013	-0.09	-0.014	-0.007	-0.044	-0.003	0.017	-0.015	0.053	-0.032	-0.013
LPJ	0.002	0.036	0	0.003	0.039	0.016	0.021	0.042	-0.023	-0.006	0.191	0.018	0.015	0.054	0.029	0.013	0.004	-0.045	-0.037	-0.017	-0.005	-0.007	0.012	0.039	-0.028	-0.006
LPX	-0.017	0.003	-0.002	-0.004	0.025	-0.001	0.009	0.025	-0.009	-0.001	-0.025	0	-0.029	0.071	0.041	-0.006	0.008	-0.002	-0.006	-0.003	-0.005	-0.009	0	-0.006	0.007	-0.003
OCN	0.003	0.016	0.001	0.013	-0.024	0.001	0.021	-0.015	0.04	-0.002	0.033	0.009	0.012	-0.007	0.018	-0.004	0.027	0.001	0.012	-0.001	0.008	-0.004	-0.003	-0.008	-0.023	0
ORCHIDEE	0.004	-0.015	-0.002	-0.011	0.05	0.003	-0.015	-0.015	-0.029	0.006	0.082	0.01	-0.005	0.034	0.072	-0.002	0.04	-0.009	-0.073	0.011	0	-0.01	-0.008	-0.013	-0.017	-0.008
VISIT	-0.009	0.017	-0.008	-0.008	-0.015	0.013	-0.019	-0.034	-0.048	-0.003	0.029	-0.008	-0.007	0.029	0.067	-0.032	0.027	-0.003	-0.014	-0.029	0.008	0.003	-0.006	-0.008	-0.001	0.002
MMEM	-0.004	0.014	0.001	0	0.016	0.001	0.012	0.002	0.011	-0.005	0.045	0.003	-0.002	0.028	0.02	-0.003	0.008	-0.009	-0.019	-0.008	-0.001	0.002	-0.004	0.008	-0.013	-0.004

e

	ASK	KEY	MID	IZO	WIS	BMW	BME	WLG	TAP	AZR	UTA	NWR	UUM	CMO	HUN	SHM	MHD	CBA	BAL	ICE	STM	BRW	SUM	MBC	ZEP	ALT
	23°N-50°N															50°N-90°N										
CLM4.5	0.003	0.001	-0.002	0	-0.008	0.002	-0.001	-0.003	0.002	0.003	-0.004	0.001	-0.004	-0.018	0.005	0.004	-0.003	0.005	0.004	-0.006	-0.007	-0.01	0.015	-0.012	-0.003	0
ISAM	0.002	0.001	-0.002	-0.001	-0.007	0.002	0	-0.003	0.004	0.003	-0.004	0	-0.004	-0.018	0.005	0.002	-0.003	0.005	0.004	-0.003	-0.007	-0.01	0.015	-0.012	-0.003	0
JULES	0.003	0.001	-0.002	0	-0.006	0.002	0	-0.003	0.003	0.004	-0.004	0	-0.004	-0.019	0.005	0.004	-0.003	0.006	0.004	-0.004	-0.007	-0.01	0.013	-0.013	-0.003	0
LPJ	0.003	0.001	-0.002	0	-0.007	0.002	0	-0.003	0.003	0.003	-0.004	0.001	-0.004	-0.018	0.005	0.002	-0.003	0.006	0.004	-0.004	-0.007	-0.01	0.014	-0.011	-0.003	0
LPX	0.002	0.001	-0.002	-0.001	-0.007	0.003	-0.001	-0.003	0.003	0.003	-0.004	0.001	-0.004	-0.019	0.005	0.004	-0.004	0.006	0.004	-0.006	-0.006	-0.01	0.014	-0.011	-0.003	0
OCN	0.003	0.001	-0.002	0	-0.007	0.002	0	-0.003	0.003	0.004	-0.004	0.001	-0.004	-0.019	0.005	0.003	-0.003	0.005	0.005	-0.005	-0.006	-0.01	0.014	-0.012	-0.002	0
ORCHIDEE	0.003	0.001	-0.002	-0.001	-0.007	0.002	-0.001	-0.003	0.003	0.004	-0.004	0.001	-0.004	-0.018	0.005	0.004	-0.004	0.005	0.004	-0.005	-0.007	-0.01	0.015	-0.012	-0.003	0
VISIT	0.002	0.001	-0.003	-0.001	-0.007	0.003	0	-0.003	0.003	0.004	-0.004	0.001	-0.004	-0.018	0.005	0.001	-0.003	0.006	0.004	-0.005	-0.007	-0.01	0.014	-0.012	-0.004	0
MMEM	0.003	0.001	-0.002	0	-0.007	0.002	0	-0.003	0.003	0.003	-0.004	0.001	-0.004	-0.018	0.005	0.003	-0.003	0.006	0.004	-0.005	-0.007	-0.01	0.014	-0.012	-0.003	0

f

	ASK	KEY	MID	IZO	WIS	BMW	BME	WLG	TAP	AZR	UTA	NWR	UUM	CMO	HUN	SHM	MHD	CBA	BAL	ICE	STM	BRW	SUM	MBC	ZEP	ALT
	23°N-50°N															50°N-90°N										
CLM4.5	-0.03	-0.014	0.005	-0.034	-0.027	0.009	-0.056	-0.025	-0.027	0.009	-0.038	0.003	0.115	0.037	-0.108	0.011	0.104	-0.026	0.01	-0.058	0.009	-0.016	-0.029	-0.152	0.047	0.018
ISAM	-0.011	-0.029	-0.015	-0.038	-0.063	-0.01	-0.07	-0.015	-0.118	0.016	-0.041	0.023	0.028	0.003	0.035	-0.025	-0.031	-0.026	0.018	-0.048	0.035	-0.022	0.037	-0.107	0.048	0.024
JULES	0.074	-0.043	-0.022	-0.045	-0.125	-0.028	-0.095	-0.022	-0.099	0.043	-0.023	0.029	-0.015	-0.048	0.073	-0.05	0.064	0.042	0.023	-0.065	0.031	-0.011	0.031	-0.13	0.049	0.033
LPJ	0.039	-0.008	0.004	-0.026	-0.034	0.019	-0.072	-0.109	-0.055	-0.029	-0.167	-0.035	0.08	-0.012	-0.036	0.049	0.039	-0.069	0.09	-0.042	-0.01	-0.021	-0.043	-0.077	0.021	0.006
LPX	-0.029	0.005	0.009	-0.012	0.036	-0.007	0.027	0.014	-0.03	-0.023	-0.038	-0.007	0.068	-0.006	-0.151	0.025	0.001	-0.007	-0.004	-0.026	0.011	-0.004	-0.028	-0.047	-0.003	0
OCN	0.037	-0.003	0.025	-0.017	0.002	0.014	0.029	0.002	-0.125	-0.024	-0.046	-0.004	0.081	0.01	-0.078	0.013	0	-0.019	-0.027	-0.022	-0.003	0.004	-0.011	-0.007	-0.003	0.006
ORCHIDEE	0.043	0.035	0.059	-0.008	0.083	0.044	0.114	0.11	-0.03	-0.078	-0.109	-0.037	0.153	0.144	-0.17	0.118	-0.019	0.016	0.106	-0.04	-0.012	0.004	-0.027	0.154	-0.054	-0.018
VISIT	-0.055	-0.034	0.007	-0.027	-0.016	0.012	-0.029	-0.104	-0.078	-0.003	-0.04	-0.011	0.094	-0.083	-0.106	0.002	0.121	-0.022	-0.017	-0.068	-0.004	-0.01	0.001	-0.052	-0.007	0.004
MMEM	0.008	-0.011	0.009	-0.026	-0.018	0.007	-0.019	-0.019	-0.07	-0.011	-0.063	-0.005	0.075	0.006	-0.067	0.018	0.035	-0.014	0.025	-0.046	0.007	-0.01	-0.008	-0.052	0.012	0.009

Figure S13 Spatial distribution of trends in net biome productivity (NBP) (a), gross primary productivity (GPP) (b) and total ecosystem respiration (TER) (c) from September to March for eight Trendy models driven by rising CO_2 only. Note that the period from September to March corresponds to the carbon release period (CRP) of most northern temperate and boreal stations. Regions with mean annual NDVI (AVHRR NDVI3 g dataset) less than 0.1 were masked. The study period is from 1980 to 2012.

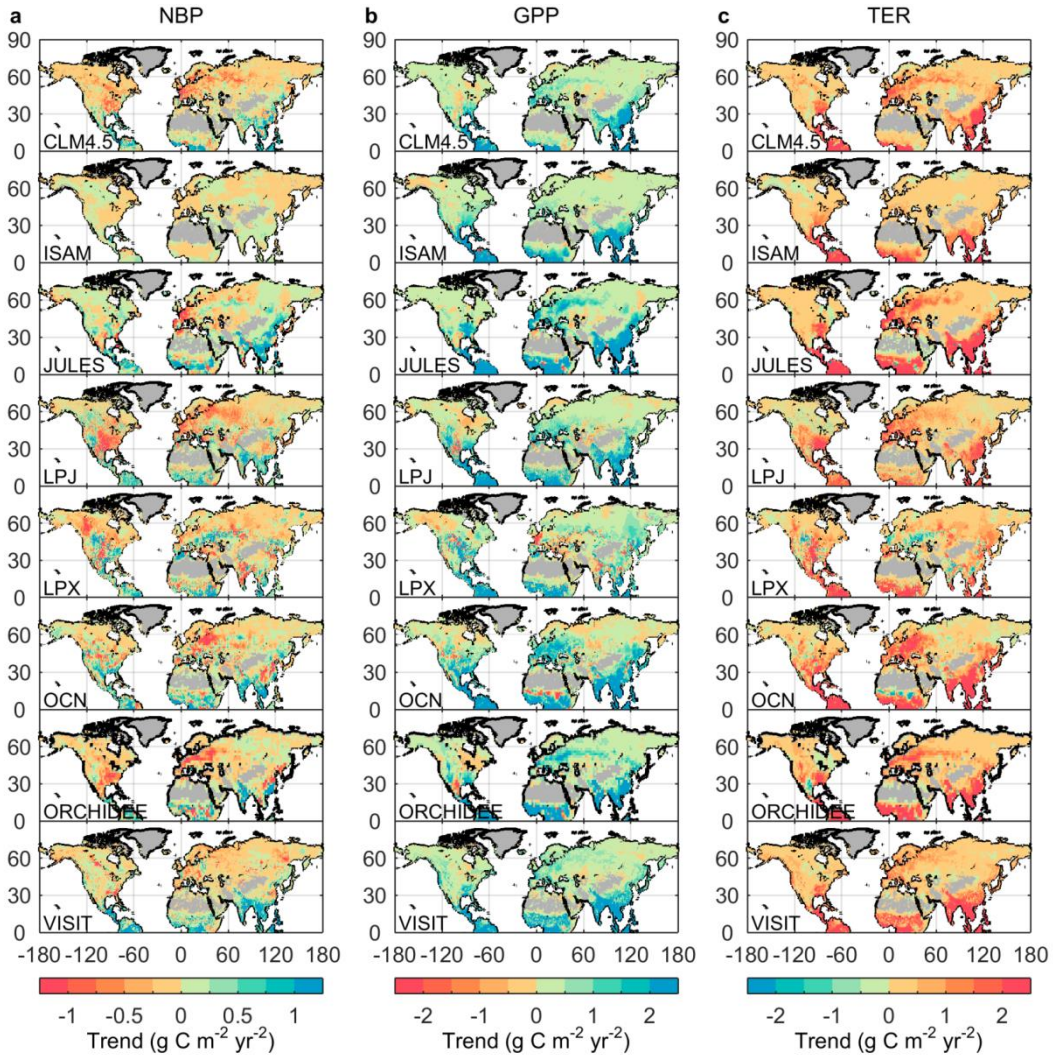

References

Clark, D. B., Mercado, L. M., Sitch, S., Jones, C. D., Gedney, N., Best, M. J., ... & Cox, P. M. (2011). The Joint UK Land Environment Simulator (JULES), model description -Part 2: carbon fluxes and vegetation dynamics. Geoscientific Model Development, **4**, 701-722.

Jain, A. K., Meiyappan, P., Song, Y., & House, J. I. (2013). CO_2 emissions from land-use change affected more by nitrogen cycle, than by the 9 choice of land-cover data. Global Change Biology, **19**, 2893–2906.

Kato, E., Kinoshita, T., Ito, A. & Yamagata, Y. (2013). Evaluation of spatially explicit emission scenario of land-use change and biomass burning using a process-based biogeochemical model. Journal of Land Use Science, **8**, 104-122.

Krinner, G., Viovy, N., de Noblet-Ducoudré, N., Ogée, J., Polcher, J., Friedlingstein, P., ... & Prentice, I.C. (2005). A dynamic global vegetation model for studies of the coupled atmosphere-biosphere system. Global Biogeochemical Cycles, **19**, 1-33.

Oleson, K. W., Lawrence, D.M., Gordon, B., Drewniak, B., Huang, M. Koven, C. D., … & Yang Z. (2013). Technical Description of version 4.5 of the Community Land Model (CLM). NCAR Technical Note NCAR/TN 503+STR; The National Center for Atmospheric Research (NCAR): Boulder, CO.

Sitch, S., Smith, B., Prentice, I. C., Arneth, A., Bondeau, A., Cramer, W., ... & Venevsky, S. (2003). Evaluation of ecosystem dynamics, plant geography and terrestrial carbon cycling in the LPJ dynamic global vegetation model. Global

Change Biology, **9**, 161-185.

Smith, B., Prentice, I. C., & Sykes, M. T. (2001). Representation of vegetation dynamics in the modelling of terrestrial ecosystems: comparing two contrasting approaches within European climate space. Global Ecology and Biogeography, **10**, 621–637.

Stocker, B. D., Roth, R., Joos, F., Spahni, R., Steinacher, M., Zaehle, S., Bouwman, L., & Prentice, I. C. (2013). Multiple greenhouse-gas feedbacks from the land biosphere under future climate change scenarios. Nature Climate Change, **3**, 666-672.

Zaehle, S. & Friend, A. D. (2010). Carbon and nitrogen cycle dynamics in the O-CN land surface model: 1. Model description, site-scale evaluation, and sensitivity to parameter estimates. Global Biogeochemical Cycles, **24**, GB1005.